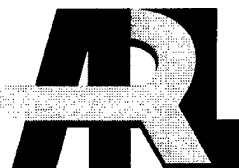


Army Research Laboratory



**Narrow Band Susceptibility Prediction
From the Impulse Scatter Response
of a Pseudomissile (Case I)**

**By Jayme B. Henderson
Survivability/Lethality Analysis Directorate
Information & Electronic Protection Division**

ARL-TR-1035

April 1998

Approved for public release. Distribution unlimited.

19980710 117

DTIC QUALITY INSPECTED 1

The findings in this report are not to be construed as an official Department of the Army position unless so designated by other authorized documents.

Citation of manufacturer's or trade names does not constitute an official endorsement or approval of the use thereof.

REPORT DOCUMENTATION PAGE		Form Approved OMB No. 0704-0188	
Public reporting burden for this collection of information is estimated to average 1 hour per response, including the time for reviewing instructions, searching existing data sources, gathering and maintaining the data needed, and completing and reviewing the collection of information. Send comments regarding this burden estimate or any other aspect of this collection of information, including suggestions for reducing the burden to Washington Headquarters Services, Directorate for Information Operations and Reports, 1215 Jefferson Davis Highway, Suite 1204, Arlington, VA 22202-4302 and to the Office of Management and Budget, Paperwork Reduction Project (0704-0188), Washington, DC 20503.			
1. AGENCY USE ONLY (Leave Blank)	2. REPORT DATE April 1998	3. REPORT TYPE AND DATES COVERED Final Report (1993 - 1995)	
4. TITLE AND SUBTITLE Narrow Band Susceptibility Prediction From the Impulse Scatter Response of a Pseudomissile (Case I)		5. FUNDING NUMBERS	
6. AUTHOR(S) Jayme B. Henderson		8. PERFORMING ORGANIZATION REPORT NUMBER ARL-TR-1035	
7. PERFORMING ORGANIZATION NAME(S) AND ADDRESS(ES) U.S. Army Research Laboratory Survivability/Lethality Analysis Directorate ATTN: AMSRL-SL-EP White Sands Missile Range, NM 88002-5513		10. SPONSORING/MONITORING AGENCY REPORT NUMBER ARL-TR-1035	
9. SPONSORING/MONITORING AGENCY NAME(S) AND ADDRESS(ES) U.S. Army Research Laboratory 2800 Powder Mill Road Adelphi, MD 20783-1145			
11. SUPPLEMENTARY NOTES			
12a. DISTRIBUTION/AVAILABILITY STATEMENT Approved for public release; distribution unlimited.		12b. DISTRIBUTION CODE A	
13. ABSTRACT (Maximum 200 words) A comparison is made between the narrow band signal coupled into and the impulse signal scattered from a pseudomissile (case I) test object. Simple linear scattering measurement techniques and computational algorithms are presented for the extraction and processing of the scattered signal. The information collected consists of the modal response of the test object to the incident electromagnetic field. A comparison of this impulse scatter data and the narrow band coupling data shows that, for the pseudomissile test object, the scattered and coupled data have a good mode correlation.			
14. SUBJECT TERMS impulse, scatter, ultra-wide band, coupling		15. NUMBER OF PAGES 93	
		16. PRICE CODE	
17. SECURITY CLASSIFICATION OF THIS REPORT UNCLASSIFIED	18. SECURITY CLASSIFICATION OF THIS PAGE UNCLASSIFIED	19. SECURITY CLASSIFICATION OF ABSTRACT UNCLASSIFIED	20. LIMITATION OF ABSTRACT SAR

Preface

The following report is the product of several years of development, beginning in 1993 and extending through December 1995. Physical measurements were performed to determine whether a relation existed between the signal coupled to a system and its impulse scatter response.

Early efforts at the U. S. Army Research Laboratory's (ARL) Electromagnetic Analysis Facility (EMAF), located at White Sands Missile Range (WSMR), NM, have focused on simple theoretical coupling codes which provided fundamental insights into missile coupling. Until the recent development of the pseudomissile coupling code by Clemson University in South Carolina, the data generated by these earlier codes did not provide physical voltage levels coupled to a system component. The coupling code has been validated by physical measurements in the EMAF. In spite of the applicability to missile body shapes, none of these codes is suited to composite or nonmissile-shaped housings for electromagnetic (EM) field-sensitive electronic components. In general, coupling codes have not matured sufficiently to eliminate the need for physical electromagnetic interference (EMI) measurements.

This report is limited in scope to the pseudomissile model. This effort has sought to provide a better understanding of the relation between the EM frequencies scattered from and those frequencies coupled to a simple detection circuit mounted to the pseudomissile. This is done through the use of physical measurements of both narrow band coupled and wideband scattered EM fields. In addition to the measurements, a comparison is made with calculated values. Due to the difficulty of the problem, this paper does not attempt to establish a relation between the magnitudes of the scattered/coupled fields.

The 6.2 effort presented in this report demonstrates improvement of tools, techniques, and methodologies that may help in determining the EM susceptibility of U.S. Army systems in both a timely and less expensive manner. There is no cutoff date on the information.

ARL, Survivability/Lethality Analysis Directorate (SLAD), Information & Electronic Protection Division (IEPD), WSMR, NM, prepared this report. Comments and suggestions should be directed to:

Director
U. S. Army Research Laboratory
Survivability/Lethality Analysis Directorate
Information & Electronic Protection Division
(ATTN: Jayme Henderson)
White Sands Missile Range, NM 88002-5513
Commercial: (505) 678-9026, DSN: 258-9026.

Acknowledgments

This work was conducted at the U.S. Army Research Laboratory's (ARL) Electromagnetic Analysis Facility (EMAF), located at White Sands Missile Range (WSMR), NM. The author wishes to express appreciation to the facility contractors: Mr. Kelly Harbst of Syndetix, Inc., for his patience and care in the collection of the data; Mr. David Garcia of the Physical Sciences Laboratory for his fine craftsmanship in constructing the transverse electromagnetic (TEM) horn antenna used to generate the data for this report; and William Cooper of Syndetix, Inc., for his acquisition software programming, expertise in electromagnetics, and many insightful discussions. In addition to these good individuals, the work of Mr. William F. Collins has literally been instrumental in making the measurement data collection possible. Mr. Collins designed the telemetry system. Lastly, my sincerest thanks to Ms. Joy L. Arthur for her motivation and interest in this project. This project could not have been performed without any one of these people.

Contents

Preface	1
Acknowledgments	3
Executive Summary	9
1. Introduction	17
<i>1.1 Purpose</i>	18
<i>1.2 Background</i>	18
2. System Description	19
<i>2.1 Detector Diode</i>	21
<i>2.2 Telemetry Package</i>	23
3. Theory	25
4. Instrumentation	31
<i>4.1 Narrow Band</i>	31
<i>4.2 Ultra-Wide Band</i>	32
5. Experiments	39
<i>5.1 Narrow Band Coupling</i>	39
5.1.1 Calibrations	39
5.1.1.1 <i>Field Strength</i>	39
5.1.1.2 <i>Telemetry</i>	39
5.1.1.3 <i>Diode</i>	40
5.1.2 Measurements	41
<i>5.2 Wide Band Scattering</i>	43
5.2.1 Calibrations	43
5.2.1.1 <i>Coaxial Cables</i>	44
5.2.1.2 <i>EM Field</i>	44
5.2.2 Anechoic Chamber Scattering Measurements	46
5.2.3 Ground Plane Scattering Measurements	50
6. Comparison of Results	55
7. Conclusions	61
8. Recommendations	63

References65
Acronyms and Abbreviations67
Appendices	
<i>Appendix A. D-Dot Signal Integration Scaling and Correction</i>69
<i>Appendix B. Background Subtraction</i>77
<i>Appendix C. Normalization</i>81
Distribution85

Figures

1. Pseudomissile19
2. Pseudomissile cases20
3. Case I configuration21
4. Installation of the detector diode in the missile nose (cases II and III shown)22
5. Telemetry system diagram23
6. Scatter regions of a simple system25
7. Pseudomissile dimensions26
8. Brass probe above the circular frustum end cap27
9. Pseudomissile NEC 2 configuration29
10. NEC 2 bistatic scatter spectrum (solid) with scaled window function overlaid (dotted)29
11. NEC 2 computed scatter response (solid) using Blackman windowed bandlimited incident impulse (dotted)30
12. Narrow band chamber calibration instrumentation31
13. Narrow band chamber configuration32
14. Impulse scattering configuration33
15. Wide band bistatic scatter block diagram34
16. HMP1 impulse generator and TEM antenna35
17. Signal from the HMP1 impulse generator36
18. Prodyne D-dot field probe36
19. Digitizing oscilloscope37
20. Thermal drift of the measured response versus time40
21. Diode calibration setup41
22. Diode 2 input power versus frequency for a -50 dBV response on TM channel 141
23. Power density required to induce a -50 dBV TM channel 1 response42
24. Normalized susceptibility of the pseudomissile43

25. Incident field45
26. Background signal45
27. Background signal with pseudomissile scatterer48
28. Scatter response of pseudomissile48
29. Integrated scatter response48
30. Pseudomissile impulse scatter response ($K = 0.15$)49
31. Normalized bistatic scatter transfer function ($K = 0.15$)49
32. Impulse response computation algorithm50
33. Ground plane scatter geometry51
34. Scatter signal with probe present51
35. Scatter signal without probe present52
36. Difference signal between figures 34 and 3552
37. Rectangular "short-time" windowed waveform53
38. Fourier transform of the windowed difference waveform53
39. Scatter response (same as figure 31)57
40. Fourier transform of the windowed difference waveform (same as figure 38)58
41. Normalized susceptibility (same as figure 24)58
42. NEC 2 bistatic scatter analysis58

Tables

1. Missile body sensitive frequencies27
2. Missile probe sensitive frequencies28
3. Pseudomissile NEC 2 input file28
4. Pseudomissile resonant frequencies56
5. Frequency errors, Δf_c59
6. Percent bandwidth errors59

Executive Summary

Introduction

Impinging electromagnetic (EM) fields induce surface currents on the conductive housings of electronic systems. Scattered fields occur in three general regions: Rayleigh, Mie, and optical. Of these three scattering regions, the Mie (or resonance) scattering appears to have an important role in identifying dominant frequencies where the system's coupled response will be greatest. Resonant structures located near interior electronic coupling ports enhance the system's response to the EM field.

A linear Fourier analysis of the data presented in this report shows that there is a relation between the EM energy spectrum scattered and that which coupled into the pseudomissile system. It is recognized that this linear analysis is a simplification for more complex systems. Furthermore, once energy is coupled into a system, the problem becomes even more complex with the addition of apertures, cavities, dielectrics, conductors, semiconductors, and ferrite materials. However, as this paper shows, the linear approximation is appropriate to demonstrate a correlation between the scattered and coupled frequencies of the pseudomissile test system.

Purpose

This paper demonstrates the correlation of scattered impulse-like, ultra-wide band EM fields to swept frequency narrow band coupled signals. This relation is being studied to develop tools, techniques, and methodologies to determine whether coupling frequencies can be quickly identified through scattered signature data. This is done by investigating the resonance relation of the coupled EM signal to the scattered EM field.

Overview

The pseudomissile experimental model was originally designed as a self-contained validation tool for the narrow band EM coupling code developed by Clemson University for the U. S. Army Research Laboratory (ARL). The validation shows the results of the effort. [1] Four physical cases were originally planned. This report was based on results for case I.

There are several scattering regions that define the pseudomissile boundary. Two of those regions are particularly important in defining the susceptibility characteristics of the pseudomissile. The probe at the tip of the missile behaves as a thin monopole above a finite circular ground. The axial ratio of the probe was ~ 65 . The body/frustum combination behaves as a thick dipole with an axial ratio of ~ 8.5 . An estimate of the resonant frequencies for these two missile regions was made using both a "back-of-the-envelope" and singularity expansion method computations. As a simple approximation, wire modes are computed as $n\lambda/2$, where n is the mode number and λ is the wavelength of radiation. Thick wire modes are derived from the singularity expansion method (SEM). In addition to these simple codes, a wireframe model was developed using the NECWIN-Pro version 1.0 software package by Paragon Technologies (recently taken over by Nittany Scientific). This code uses Numerical Electromagnetic Code version 2 (NEC 2) at its computational core. A frequency sweep analysis was performed up to 2 GHz. The mesh size was approximately $\lambda/10$ at 1 GHz and dropped to approximately $\lambda/5$ at 2 GHz (the upper bound of the frequency sweep).

Physical measurements were conducted in the Electromagnetic Analysis Facility's (EMAF) large anechoic chamber located at White Sands Missile Range (WSMR), NM. This chamber is 93 ft long by 32 ft wide by 26 ft high. It has a rectangular quiet zone 72 ft long by 24 ft wide by 14 ft high. This facility contains the equipment necessary to make narrow band electromagnetic interference (EMI) coupling measurements over the 250 MHz to 18 GHz frequency range and is usable down to 100 MHz with appropriate calibration.

The necessary instrumentation to perform the wide band measurements was acquired by or constructed at the EMAF. The instrumentation was configured in the EMAF's large anechoic chamber. Scattering measurements were restricted to the bistatic configuration.

Scatter of EM impulses to identify system-specific resonant frequencies is used as part of the in-house development program designed to reduce the amount of time presently necessary to perform susceptibility assessments of U.S. Army systems.

To ensure the accuracy of the measured signal levels, calibrations were made of the incident field strength and coupled signal telemetry system.

The dynamic range of the coupled signal response was improved by modulating the incident radio frequency (RF) signal with a 1000 Hz square

wave. The RF power density was adjusted until a 1000 Hz coupled signal response of -50 dBV was measured with an audio signal analyzer. The power level was recorded, and the frequency was incremented. The frequency was swept across the 100 MHz to 3 GHz frequency bands and the experiment repeated. This revealed the characteristic body and probe mode resonances. Dominant response frequencies below 1 GHz were a consequence of the characteristic body modes. These occurred at ~100, 183, 300, 404, and 519 MHz. A particularly important feature of the narrow band coupling data was the strong peak above 1 GHz at 1.3 to 1.5 GHz. This frequency corresponds in part to the $\lambda/2$ resonant frequency of the small probe and its image in the frustum's circular ground plane cap. However, the dominant peak observed for the missile probe is not a clean resonance since there is likely several strong mutual interaction terms between the probe and the truncated circular edge of the frustum cap.

After the narrow band susceptibility response of the pseudomissile was measured in the EMAF's large anechoic chamber, bistatic impulse scattering measurements were conducted. The bistatic angle $\beta = 90^\circ$ was selected for two reasons. One reason was that a separation between the transmit and receive antennas allowed the placement of a large RF-absorbing barrier between the two antennas to reduce the amount of crosstalk. The second reason was that significant reradiation of the coupled energy in the form of low Q modes were expected to be observable for the given configuration. Resonant modes of higher Q would be detected best in a monostatic condition.

The incident waveform was measured by replacing the pseudomissile with the D-dot field sensor and applying the appropriate integration and scaling to the incident signal.

The D-dot field sensor was then placed in its bistatic configuration as a receive antenna and pulse radiated at the measurement volume without the pseudomissile present. The resulting background signal was measured and stored for later subtraction. The pseudomissile was then placed in the measurement volume and another measurement waveform taken. The background signal was then subtracted from the scattered plus background signal, leaving only the scattered signal and any residual noise. The scattered signal was then processed to remove the effects of the measurement system's transfer function. Within the band limits of the system, the resulting deconvolution of the scattered waveform with respect to the incident waveform yielded the impulse scatter response of the pseudomissile.

The deconvolution operation was performed in the frequency domain by dividing the scattered signal by the incident signals' frequency spectra and then inverting the quotient. The effects of high-frequency noise were reduced by applying a "singularity" filter. This was accomplished by adding a small value with an amplitude approximately equal to the noise floor of the incident signal.

The probe scatter response is not obvious in the impulse scatter data taken in the EMAF. The response of the probe was better isolated by making use of data collected on the ground plane. Prior to the development of the U.S. scatter capability at the EMAF, a series of scatter measurements was conducted at the ground plane facility in August 1994. A signal subtraction and windowing technique was applied to this data to extract the pseudomissile probe's dominant resonant frequency. This resulted in a distinct probe mode scatter response at 1.54 GHz. A detailed time-frequency, energy, and bi-time self correlation analysis of this data was made by Dr. Eric Walton of Ohio State University. [2]

Comparison of Results

Since the prediction of the coupled signal is pertinent to this discussion, the narrow band coupling data was considered to be the reference to which all other data was compared.

Comparing these frequencies with those measured shows that the $n\lambda/2$ calculated body modes are all higher in frequency than the measured body modes. This was because parasitic loading (e.g. body thickness, probe tip, end caps, and missile frustum taper) was unaccounted for in this simple calculation. The first two probe modes were computed to occur at 1.46 and 2.91 GHz. Since the thin wire approximation is applicable to the probe, the first probe mode corresponds closely to the 1.3 to 1.5 GHz susceptibility frequency observed for the pseudomissile. The second probe mode was not observed in the coupling data.

The scatter signature of the pseudomissile was computed from the impulse scatter data collected for what was considered an optimum experimental configuration. The first four or five body modes that appear in the scatter data also appear in the coupling data. The frequencies of these resonances are within about 10 MHz when compared to the coupled data.

Scattering measurements made on the ground plane allowed the isolation in time of the missile probe with its cross terms. The configuration of the experiment was not ideal. To enhance this specific response, a rectangular signal window was placed over the probe's location in time. This resulted in a well-defined response at 1.54 GHz. This frequency was higher than expected from the probe. The cause for this was due in part to the probe's mutual interaction with the small circular ground plane at the end of the pseudomissile as well as the higher order body modes.

The resonant peaks that result from these measurements are shown in the following table of resonant frequencies.

Resonant frequencies

	$n_{\lambda}/2$ calculated	SEM calculated	NEC 2 computed	Impulse scattered	Coupling measured
Body modes (MHz)					
1	112.50	88.50	90	<100*	<100*
2	225.00	190.59	190	196	183
3	337.50	295.75	280	303	300
4	450.00	402.62	380	391	404
5	562.50	510.68	560	508	519
Probe modes (MHz)					
1	1460	1313.33	not avail.	1540	1300-1500
2	2910	2722.39	not avail.	none	none

* lowest frequency measured.

The percentage bandwidth errors associated with the different methods are shown in the following table.

Percent bandwidth errors

Mode	$n_{\lambda}/2$ calculated	SEM calculated	NEC 2 computed	Impulse scattered	Coupling measured
Body modes (MHz)					
1	*	*	*	*	0
2	84	16	14	26	0
3	64	8	34	6	0
4	78	2	40	22	0
5	128	24	120	32	0
Probe modes (MHz)					
1	<32	<38	*	<48	0
2	*	*	*	none	none

* cannot be determined.

Conclusions

Two EM impulse scattering techniques are presented in this paper. The first technique included dominant body mode resonance determination by Fourier transformation of the direct time domain scatter response. The second method used a physical geometry differencing technique in which the pseudomissile scatter response was measured with the probe in place and with the probe absent. The difference of the two scattered signals was determined and a "short-time" window applied about the response time window of the probe protruding from the pseudomissile's forward end. Again, the Fourier transformation was made. This enhanced the subtle probe resonances not visible with the first direct scatter method. It was not clear whether the dominant term of the scatter spectrum was the result of the probe wire or the mutual interaction terms between the probe and the circular cap.

For the pseudomissile case considered, coupling to the missile probe was more important than body mode coupling at inducing a response in the pseudomissile. Distinct resonances appeared in the scatter transfer function, which corresponded to body modes of the system. A technique to isolate the probe response from the grosser body response was used. This allowed a clear identification of a frequency near the probe's first resonant mode but no clarity that this was indeed predominantly due to the probe.

Several numerical codes were used to provide different comparisons. The simple $n\lambda/2$ calculation of body modes produced an average error of 42 MHz. The difference between mode frequency peaks is ~ 100 MHz. It is clear that the $n\lambda/2$ calculation cannot be effectively used even for "back of the envelope" calculations for body mode resonances without including some correction for the body thickness. The singularity expansion method accounts for the thickness and had an average accuracy of ~ 5 MHz in predicting the body modes. This high degree of accuracy is expected due to the close similarity of the pseudomissile and a simple missile. The NEC 2 analysis resulted in an average body mode prediction accuracy of ~ 28 MHz. Using the magnetic field integral equations (surface patch cards) to model the solid body may have resulted in less error than the electric field integral equations (wire cards). This was not studied further.

Since the coupled susceptibility response window ranged from 1300 to 1500 MHz, the computational techniques were adequate at predicting the first resonant frequency. However, the $n\lambda/2$ calculation and singularity expansion techniques produced higher order modes which do not correspond to the

coupled data. The geometry used for the NEC 2 analysis was more representative of the pseudomissile but did not yield markedly better results than the other two computational techniques. The probe was not modeled independent of the missile body.

The impulse scattering technique resulted in a singular 1540 MHz frequency corresponding to the region containing the probe response. However, it is higher in frequency than the pseudomissile's measured 1300 to 1500 MHz susceptibility response band. It is not clear based on this method how the probe response was perturbed by the local boundary beyond the observed frequency shift.

A priori narrow band coupling information was used in this analysis to see where patterns might exist in impulse scatter data which might allow susceptibility prediction based upon the ultra-wide band scattering signature data. Although coupled resonances are clearly identifiable in the scatter spectrum with reasonable frequency prediction accuracy, there is no strong indication which resonances are most important for introducing undesirable EMI effects. In fact, an abundance of frequencies were found in the scatter data which had no apparent physical meaning in the coupling data. This was the primary reason the probe data from the ground plane measurements were analyzed.

Recommendations

The results of this report show that scattered frequencies from a missile shape do correspond to coupled response frequencies. However, there is an over abundance of scatter modes which do not show up in the physical coupling measurements. The probe removal technique was applied to the response waveform and resulted in a strong enhancement of the desired mode. This shows that impulse scattering will not likely yield coupling frequencies without more advanced signal extraction techniques. Signal extraction techniques based upon measurements, as well as development of signal processing, are necessary in order to make the ultra-wide band scatter technique into a more useful EMI investigation tool.

Since the nature of EM coupling has a scaling property for linear systems dependent upon the local region's resonant modes, it is appropriate to consider developing better analysis tools and techniques in the light of the advances in computational power. Wavelets, bi-time, Wigner, and windowed Fourier techniques have already been applied with some success. [2]

In addition to the improvement of signal processing techniques, it was demonstrated with the ground plane data that if appropriate measurement techniques or methods are applied, subtle but highly important information can be pulled from the scatter data. The way this data is processed can be improved by applying better windowing, signal subtraction, and modal decomposition such as the singularity expansion method.

Improvement of tools, techniques, and methods employed to extract the resonance information would lay the groundwork for accurately predicting the susceptibility frequencies for more complex systems. To promote a methodical investigation of the scatter/couple relation and development of a more robust tool, further study and refinement of the increasingly complex pseudomissile (cases II - IV) is recommended.

To improve the dynamic range of the received signal, development of a better background cancellation method should be incorporated into the measurement system.

The transfer function of the scattering system has an effective bandwidth of about 3.5 GHz. This could be improved with higher bandwidth transmit and receive antennas. This will improve the bandwidth to about 5 to 6 GHz with the present pulser. With increased antenna sensitivity, a lower voltage impulse generator with wider bandwidth would improve the channel bandwidth.

It is recommended that a better theoretical as well as physical basis be examined for existing EMI data on real systems. Experience shows that there are typically only a few frequencies which dominate a system's susceptibility response profile. It would be important to determine why these modes are predominantly coupled by the system. The pseudomissile would be a good vehicle to study these filtering effects.

1. Introduction

Incident electromagnetic (EM) fields, whether intentional or unintentional, induce surface currents on the conductive housings of electronic systems. Leakage through apertures and seams in the system's skin couples to internal circuitry that can upset the normal operation of the system. Leakage is strongest when surface currents associated with incident fields are resonant with a structure that is coupled to the leakage port.

EM scattering from a body is classified into three regions. Low-frequency fields scatter quasi-statically ($\lambda \gg$ scatterer's dimension). This region is referred to as the "Rayleigh region." Mid-frequency fields scatter in a resonant manner ($\lambda \sim$ scatterer's dimension). Nomenclature for this region is the "Mie region." High-frequency EM fields scatter in a quasi-optical manner ($\lambda \ll$ scatterer's dimension). This is known as the "optical region." These scatter regions are correlated to coupled signals in a pseudomissile test body. Of the three scattering/coupling mechanisms, resonance scattering plays the most important role in identifying dominant coupling frequencies where the system's coupling response will be greatest.

Impinging EM waves generate a voltage bias across nonlinear junctions whether quasi-static, resonant, or optical exposure occurs. If these waves are appropriately modulated, this coupled signal will compete with the normal operational signals for control of the system. When this occurs, the system is susceptible to the interfering signal. Resonant structures located near coupling ports to a system's interior electronics will enhance a system's response to the EM field. Performance degradation occurs with severe interference. The severity of the interference will be strongly dependent upon the type of system to which the interfering signal couples. For example, in order to capture the phase locked loop in a frequency modulation (FM) receiver, the interfering signal must exceed a jammer-to-signal ratio (J/S) of 1. In some cases, if the fields are sufficiently large, a system malfunction can occur. This may occur through several mechanisms. Alteration of the bias levels in a circuit may cause the affected circuit to become unstable, causing the system to malfunction, shut down completely, or burn out. High power levels, such as those which occur with nuclear electromagnetic pulse (EMP), burn out unprotected circuitry.

A pseudomissile-shaped test object was chosen as an EM coupling study platform by the U.S. Army Research Laboratory's (ARL) Information & Electronic Protection Division (IEPD). This paper shows there is a resonance

relation between the narrow band coupled and wide band scattered EM fields. With further development, these techniques may be applied to predicting the susceptibility of more complex objects.

1.1 Purpose

The U.S. Army uses an extensive array of complex electronic equipment in its arsenal. Some of this equipment may be susceptible or even vulnerable to the battlefield EM radiation environment. Tools, techniques, and methodologies are being developed for the expedient identification of undesirable signal coupling by carefully investigating the resonance relation of the coupled to the scattered EM field.

1.2 Background

Electromagnetic interference (EMI) is of concern to any electronic systems design engineer. This is of particular concern to the U.S. Army when weapon systems fail to function properly on the battlefield due to intentional or unintentional EM coupling to the system electronics. A linear Fourier analysis of the data presented in this report shows that there is a relation between the scattered EM energy spectrum and that which coupled into the pseudomissile. It is recognized that a linear analysis is a simplification for the generalized EMI problem. However, as this paper shows, the linear approximation is appropriate to demonstrate a correlation between the scattered and coupled EM responses of the pseudomissile.

2. System Description

The pseudomissile experimental model shown in figure 1 was originally designed as a self-contained validation tool in conjunction with the narrow band EM coupling code developed by Clemson University for ARL. A key feature of the model was the missile probe. By incorporating the probe as part of the coupling model, it became possible to accurately measure the system's modeled response.

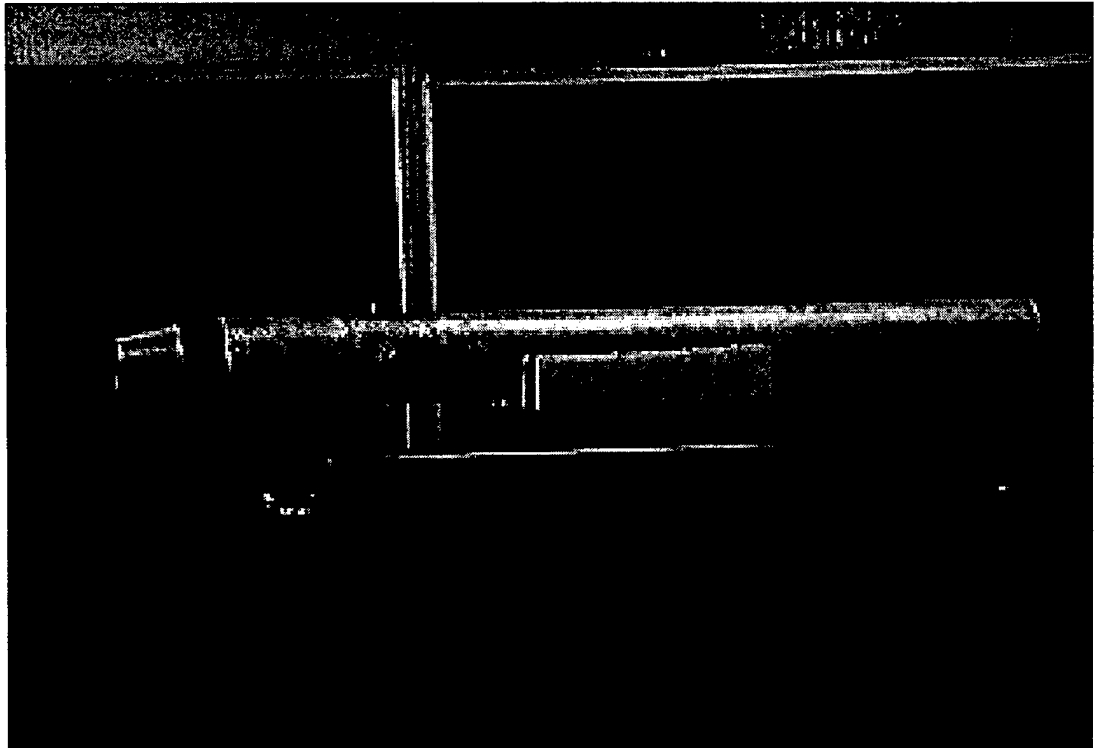


Figure 1. Pseudomissile.

A single detection junction with a known input impedance of 50 ohms (Ω) was incorporated between the conductive probe and the missile's main body. For narrow band susceptibility measurements, the coupled field was detected, and the voltage that resulted was amplified and digitized. The experimental model contains a telemetry (TM) transmitter which was fiberoptically linked to a receiver decommutator. Fiber-optic transmission of the telemetry signal allowed coupling measurements to be conducted without EM perturbation.

Four experimental cases were originally planned for study. Validation data has been collected on the first three cases. Case I consists of only an exterior boundary problem where no cavities exist in the pseudomissile. Each

subsequent case is designed with increased complexity to enable accurate validation. Case II moved the probe and bulkhead interior to the nose cone frustum while keeping the probe length shorter than the depth of the cavity. This introduced a cavity into the missile body. Case III extends the probe wire in length so that it protrudes beyond the aperture in the frustum. Case IV places a rectangular fin slot in the missile body above the interior bulkhead so that two coupling apertures are present into the cavity. These cases are depicted in figure 2. This report was based on a study of case I. The construction of case I is shown with more descriptive detail in figure 3.

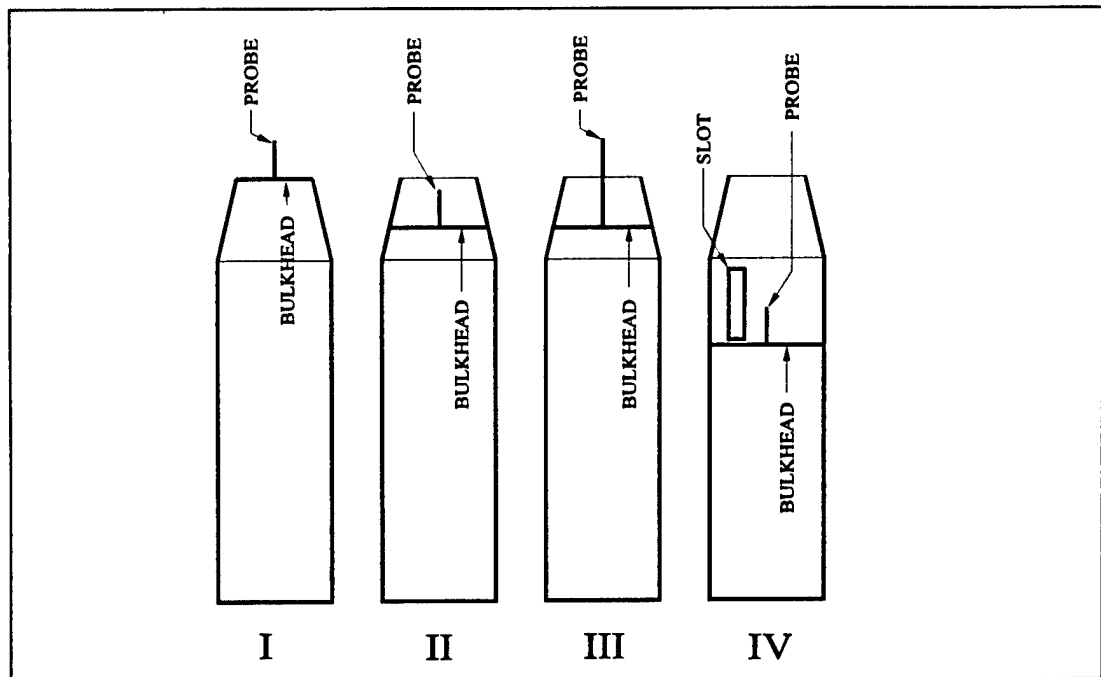


Figure 2. Pseudomissile cases.

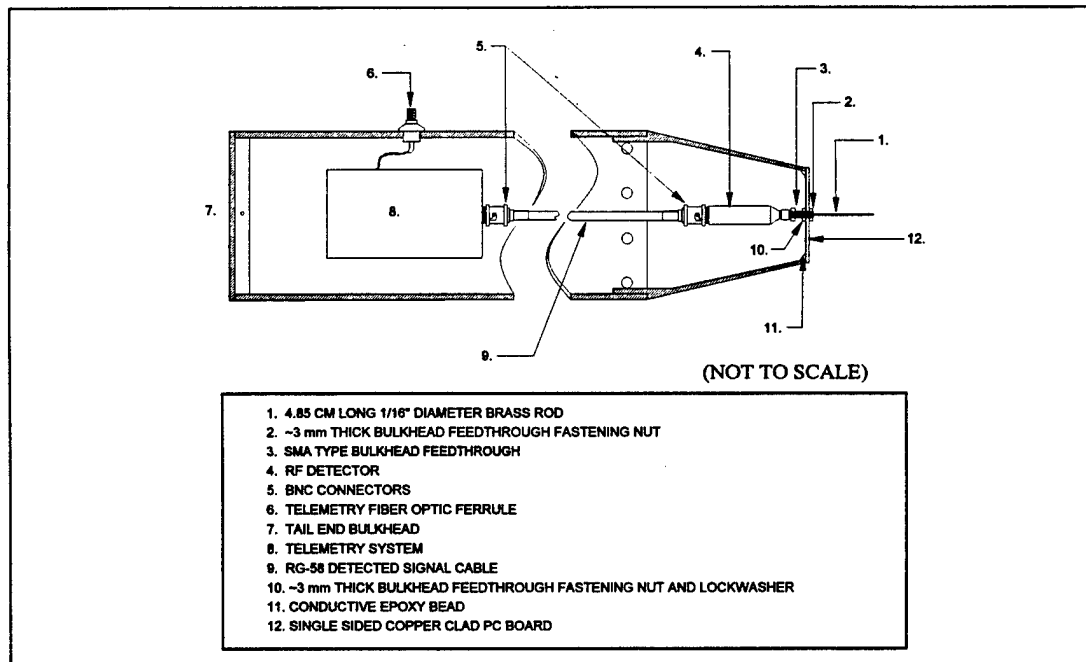


Figure 3. Case I configuration.

2.1 Detector Diode

The 50 Ω broadband MIDISCO brand radio frequency (RF) crystal detector was connected to the missile bulkhead feedthrough, as shown in figure 4. The probe was constructed with a 1/16 in. diameter brass brazing rod. Envelope detection occurs in the crystal diode, which was then amplified and digitized for telemetering to the measurement equipment. The diode response characteristic is discussed in section 5.1.1.



Figure 4. Installation of the detector diode in the missile nose (cases II and III shown).

2.2 Telemetry Package

The pseudomissile is equipped with a 12-bit serial TM transmitter and receiver pair originally designed and constructed at the Electromagnetic Analysis Facility (EMAF) as part of a compact broad band RF field probe. [3] This system transmits four channels (channels 0-3) of time division multiplexed (TDM) data over a fiber optic link. Only channel 1 was used for the narrow band susceptibility measurements. This channel has a nominal signal voltage gain of 100. A sketch of the signal conversion and telemetry system is shown in figure 5.

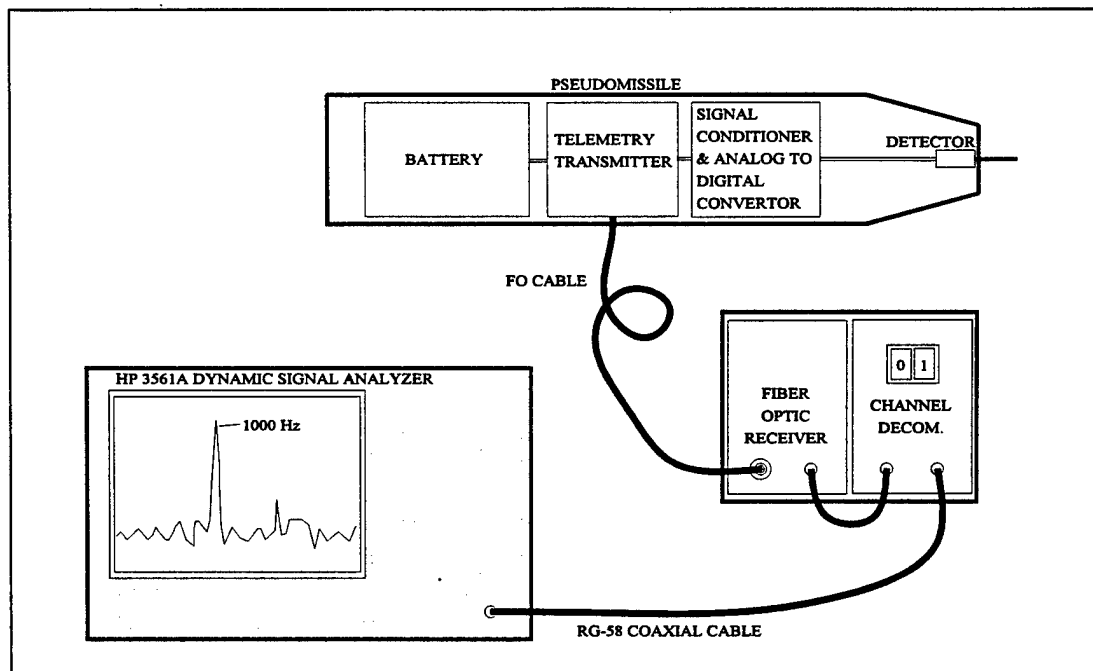


Figure 5. Telemetry system diagram.

3. Theory

A system consists of a set of scatter regions (or centers). These scatter centers are defined by local changes in the EM surface impedance of the scattering body. For large and abrupt impedance changes, the scatter centers are clearly defined. Each scatter region or pair of regions has resonant modes corresponding to the local boundary conditions. Figure 6 shows several regions of different scale for the pseudomissile system considered in this report.

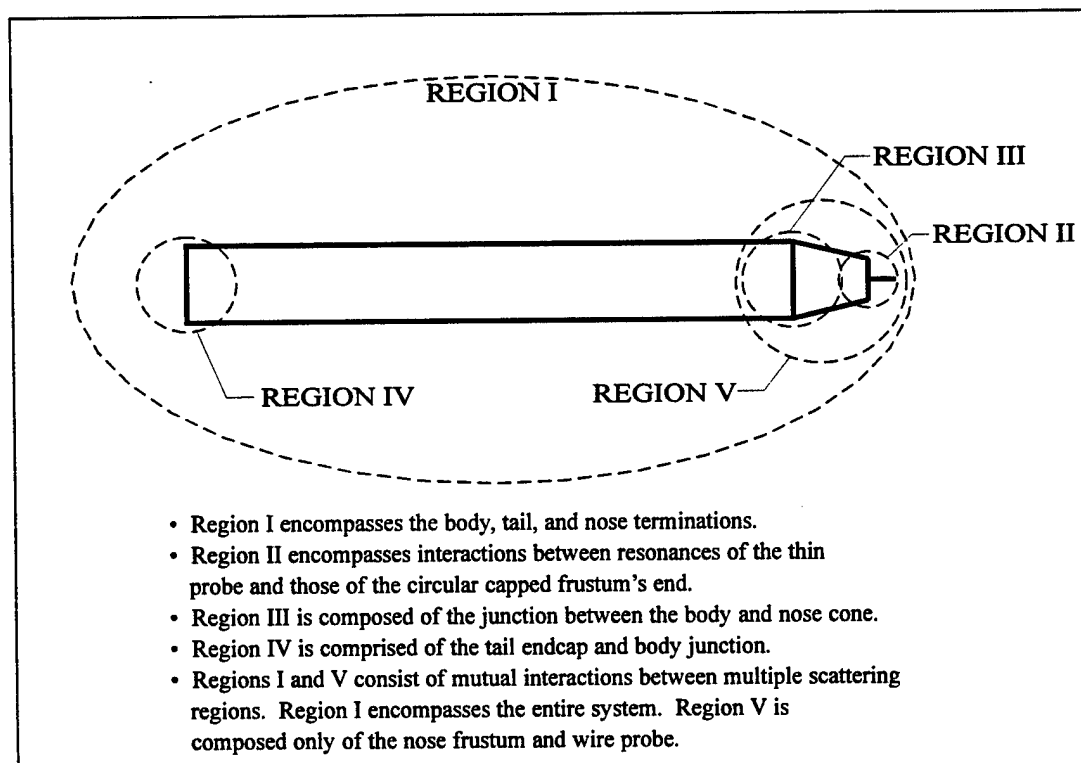


Figure 6. Scatter regions of a simple system.

When analyzing the system's expected response to an incident field, the resonant structure size with respect to the incident wavelength and the mutual interactions between regions is important. As will be seen at the conclusion of this report, modal interactions with regions I and II dominated the pseudomissile response. In general, highly dispersive structures, such as high Q cavities, will have strong mutual interactions of their impulse responses. For this report, a linear analysis was made that assumed local interactions were isolated to a small scatter region. This turned out to be invalid even for the pseudomissile, even though it contained no high Q energy storing cavities. The mutual interaction terms between the pseudomissile probe and its ground plane do not appear to be negligible. This led to an ambiguity in the most important

coupling mode frequency. The pseudomissile and the probe behave as the predominant coupling sources to the probe's load.

The pseudomissile dimensions are shown in figure 7. The body/frustum combination of the pseudomissile (region I) behaves as a fat dipole with an axial ratio of ~8.5. The probe at the tip of the missile and its image (region II) have an axial ratio of 65. The probe and its image behave as a dipole, as figure 8 depicts. With the dimensions of figure 7, a rough estimate of the resonant frequencies for these two missile regions can be made (with no compensation for axial ratio):

Body modes (region I)

$\lambda/2 = 133.30$ cm	→	f = 112.50 MHz
$1\lambda = 133.30$ cm	→	f = 225.00 MHz
$3\lambda/2 = 133.30$ cm	→	f = 338.00 MHz
$2\lambda = 133.30$ cm	→	f = 450.00 MHz

Probe modes (region II)

$\lambda/2 = 10.30$ cm	→	f = 1.46 GHz
$1\lambda = 10.30$ cm	→	f = 2.91 GHz

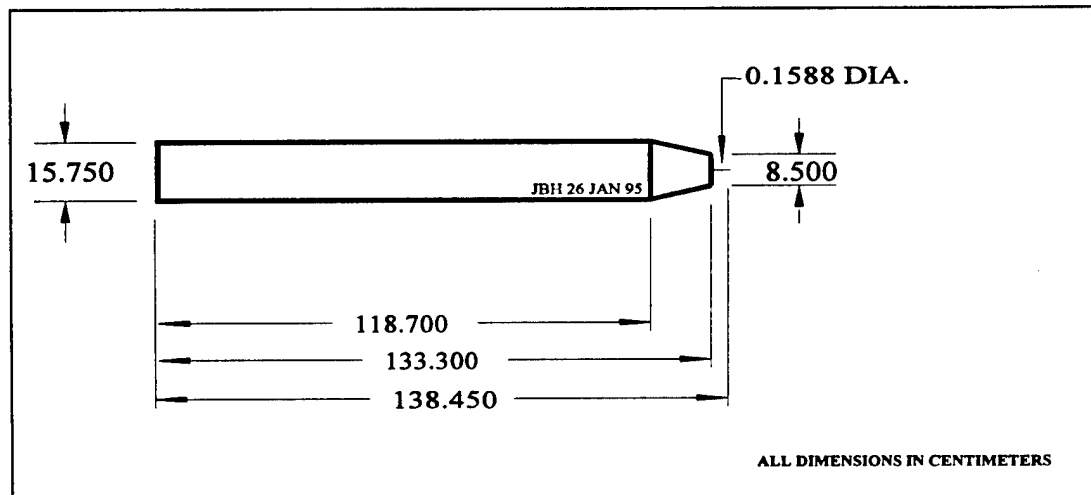


Figure 7. Pseudomissile dimensions.

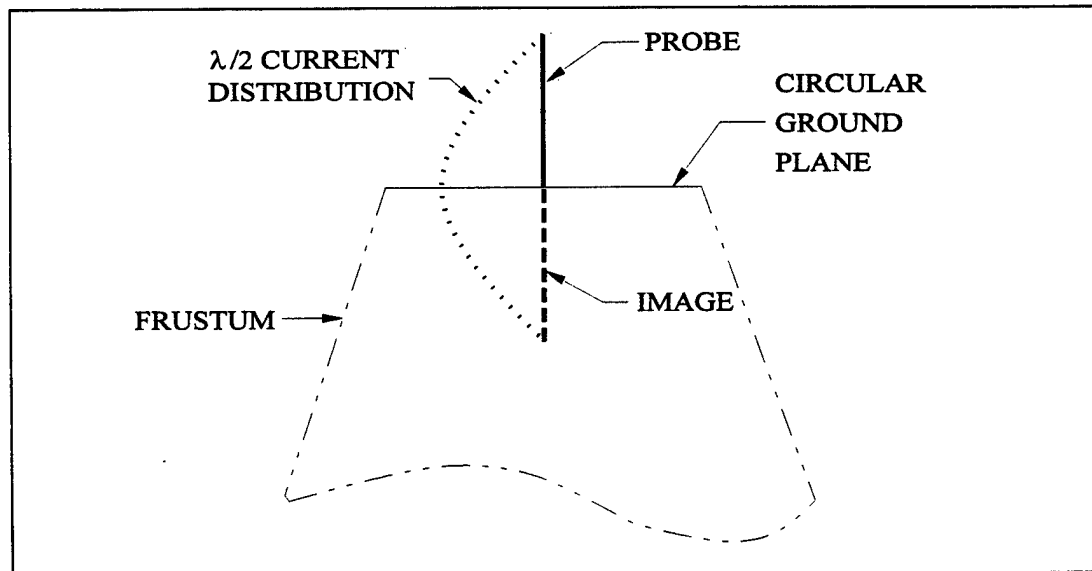


Figure 8. Brass probe above the circular frustum end cap.

The actual body modes will be lower in frequency due to the relatively large axial ratio of ~ 8.5 . Since the axial ratio of the probe and its image was large (>60), the probe effectively acts as a thin wire antenna.

The Missile Sensitive Frequency Program (MSFP) was developed for the U.S. Army EMAF (then the Electronic Warfare Vulnerability Assessment Facility, EWVAF) in 1981 to compute the effects of "thickness loading" on the missile's susceptibility response observed. [4,5] This program was used to compute the responses for both the pseudomissile body and its probe. The resulting constant threshold responses are given in tables 1 and 2.

Table 1. Missile body sensitive frequencies

Low (MHz) 3 dB down	Center frequency (MHz)	High (MHz) 3 dB down
72.64	88.55	104.47
163.39	190.59	217.78
258.88	295.75	332.62
356.88	402.62	448.36
456.57	510.68	564.79
557.50	619.65	681.80

Standard response (threshold) case

Length of the missile	1.3330 m
Diameter of the missile	0.1570 m
Aspect ratio (diameter/length)	0.1178

Table 2. Missile probe sensitive frequencies

Low (MHz) 3 dB down	Center Frequency (MHz)	High (MHz) 3 dB down
1184.16	1313.33	1442.49
2529.14	2722.39	2915.63

Standard response (threshold) case

Length of the missile	0.1030 m
Diameter of the missile	0.0016 m
Aspect ratio (diameter/length)	0.0154

The last model run on the pseudomissile was the Numerical Electromagnetic Code version 2 (NEC 2). A wire frame mesh model was used to define the pseudomissile outer shell. The input parameters are given in table 3. The user interface was developed by Paragon Technology, Inc., and sold as NECWin-Pro. This program also contains a wire mesh display feature, which was used to generate the wire missile shown in figure 9.

Table 3. Pseudomissile NEC 2 input file

CM Pseudomissile									
CE									
GW	2	5	0.0001	-0.65	0	0.075	-0.65	0	0.01
GW	3	40	0.075	-0.65	0	0.075	0.51	0	0.001
GW	4	5	0.075	0.51	0	0.04	0.65	0	0.001
GW	5	5	0.04	0.65	0	0.002	0.65	0	0.0005
GA	6	1	0.015	0	20	0.001			
GA	7	1	0.030	0	20	0.001			
GA	8	1	0.045	0	20	0.001			
GA	9	1	0.060	0	20	0.001			
GA	10	1	0.075	0	20	0.001			
GM	1	40	0	0	0	0	0.029	0	10
GM	0	0	0	0	0	0	-0.65	0	6
GA	50	1	0.04	0	20	0.001			
GM	0	0	0	0	0	0	0.65	0	50
GA	51	1	0.047	0	20	0.001			
GM	0	0	0	0	0	0	0.622	0	51
GA	52	1	0.054	0	20	0.001			
GM	0	0	0	0	0	0	0.594	0	52
GA	53	1	0.061	0	20	0.001			
GM	0	0	0	0	0	0	0.566	0	53
GA	54	1	0.068	0	20	0.001			
GM	0	0	0	0	0	0	0.538	0	54
GW	55	5	0.001	0.651	0	0.001	0.7045	0	0.0001
GW	56	1	0.001	0.7045	0	0.0001	0.7045	0	0.0001
GW	57	1	0.001	0.651	0	0.0001	0.651	0	0.0001
GM	0	0	90	0	0	0	0	0	0
GR100 18									
GE 0									
PT -1									
EX	1	1	1	1	45	0	0	1	1
FR	0	19	0	0	210	10			
RP	0	1	1	1000	45	180	1	1	6
EN									

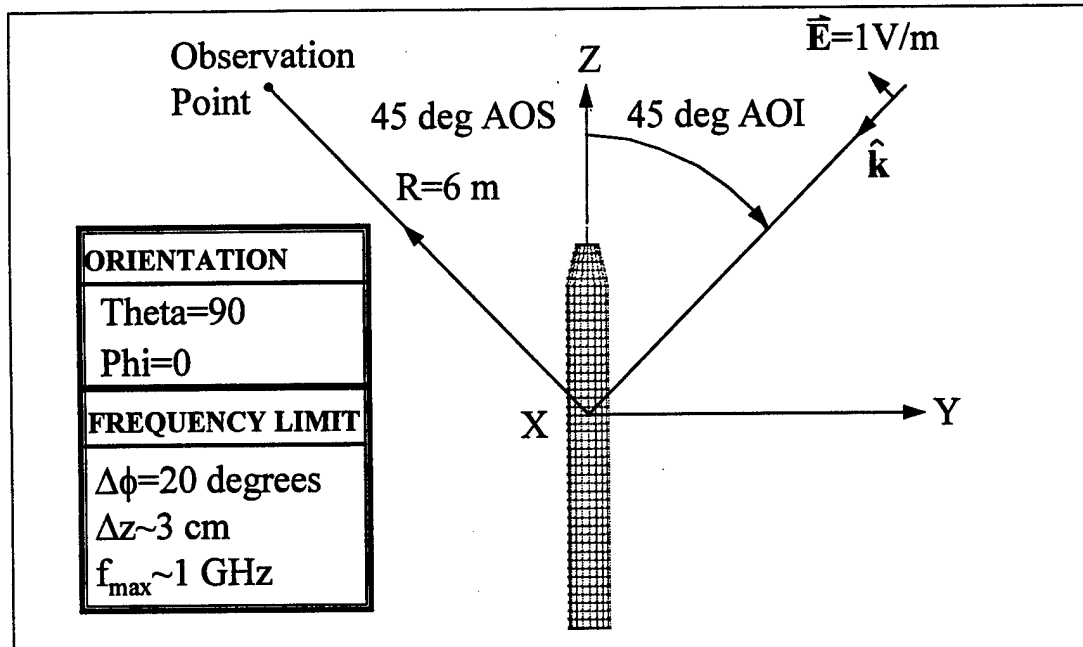


Figure 9. Pseudomissile NEC 2 configuration.

The mesh resolution allowed wire segments to be $\lambda/10$ up to 1 GHz. The frequency sweeps extended from 10 MHz to 2 GHz in 10 MHz steps. The mesh was $\lambda/5$ at 2 GHz and so does not meet the $\lambda/10$ criteria for modeling accuracy. The configuration of figure 9 resulted in the scattered field levels plotted in figure 10. A vertically scaled Blackman window function (dotted line) is overlaid. The spectrum shown is not weighted at this point.

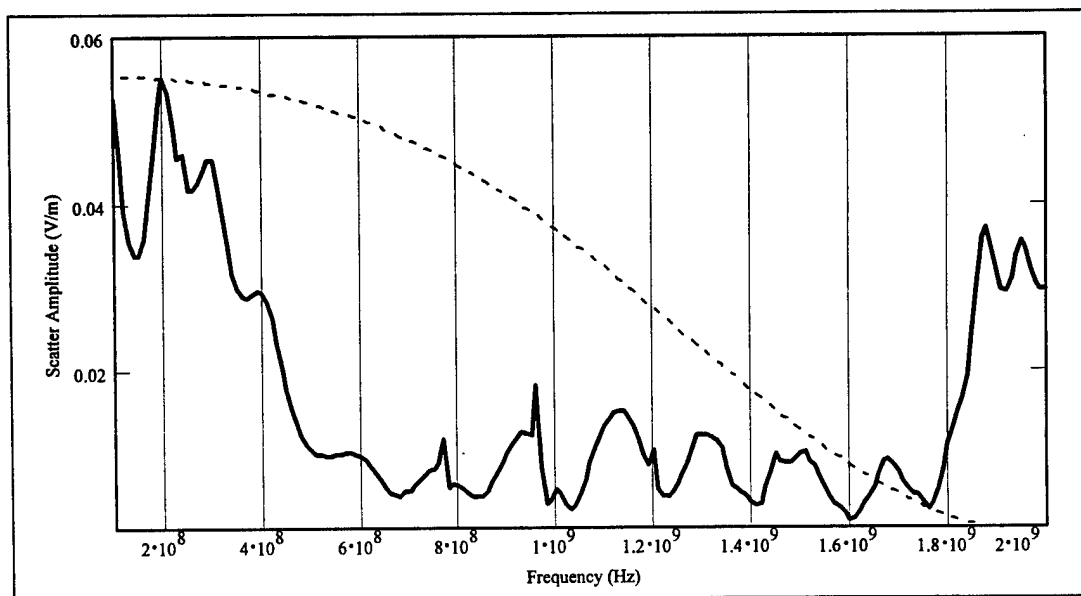


Figure 10. NEC 2 bistatic scatter spectrum (solid) with scaled window function overlaid (dotted).

The dotted line is the Blackman window of the form

$$W_j = -0.42 + 0.5\cos\left(\frac{2\pi}{N-1}j\right) - 0.08\cos\left(\frac{4\pi}{N-1}j\right) + 1 \quad (1)$$

where

W is the weighting factor applied to element j

j is the element of the amplitude scatter array, and

N is a window-width factor defined to be equal to twice the number of data points in the scatter array ($N = 400$ in this case).

Since there was only 200 data points in the spectrum, zero-padding was applied to extend the number of data points to 512 after windowing, so the inverse fast Fourier transform was applied. The resulting impulse scatter response is shown in figure 11. The appearance of the initial scatter signal ~ 18 ns into the time record is due to the ~ 6 m displacement of the observation point from the center of the scatterer (3 ns/m). The dotted line is the equivalent windowed impulse being scattered from the pseudomissile.

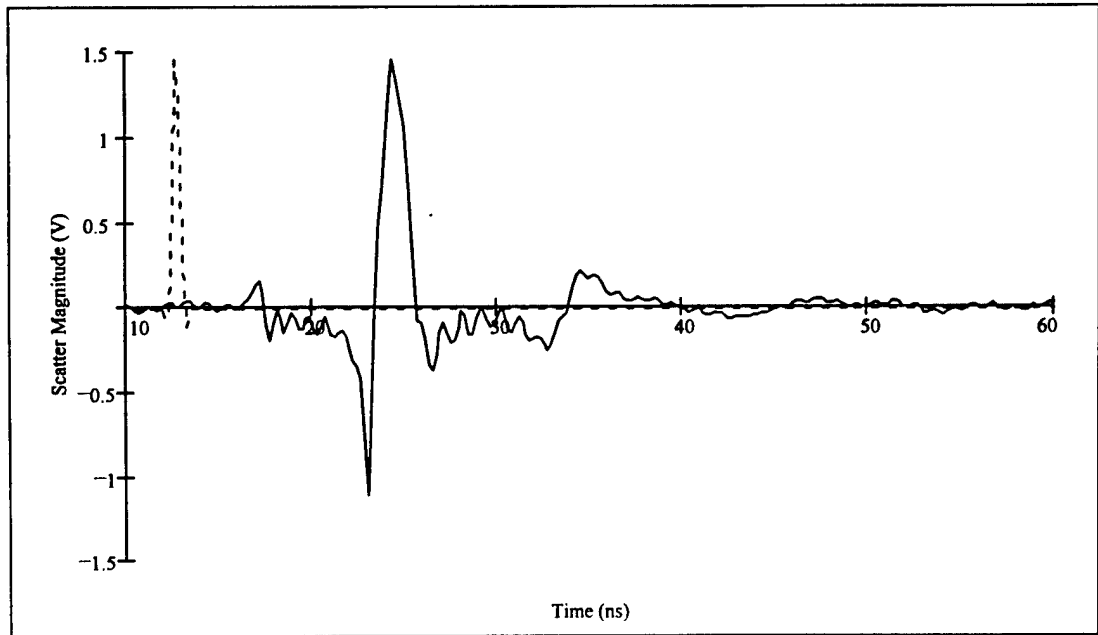


Figure 11. NEC 2 computed scatter response (solid) using Blackman windowed bandlimited incident impulse (dotted).

4. Instrumentation

These measurements were conducted in the EMAF's large anechoic chamber located at WSMR. This chamber is 93 ft long by 32 ft wide by 26 ft high. It has a rectangular quiet zone 72 ft long by 24 ft wide by 14 ft high. This facility contains the equipment necessary to make narrow band EMI coupling measurements over the 250 MHz to 18 GHz frequency range and is usable down to 100 MHz with appropriate calibration. [6]

4.1 Narrow Band

The narrow band instrumentation used for these measurements was typical for EM coupling measurements. Two standard dipoles, a Stoddart model 91870-2 for the 100 to 400 MHz band and model 91598-2 for the 400 MHz to 1 GHz band, were used to calibrate the field incident at the pseudomissile center. The calibration transmit antenna used from 100 MHz to 1 GHz was a log-periodic dipole array antenna. Standard gain horns were used for the calibration measurements across the 1 to 3 GHz bands. A typical chamber configuration for the narrow band calibrations is shown in figure 12. Narrow band chamber calibration is discussed in detail in section 5.1.1.

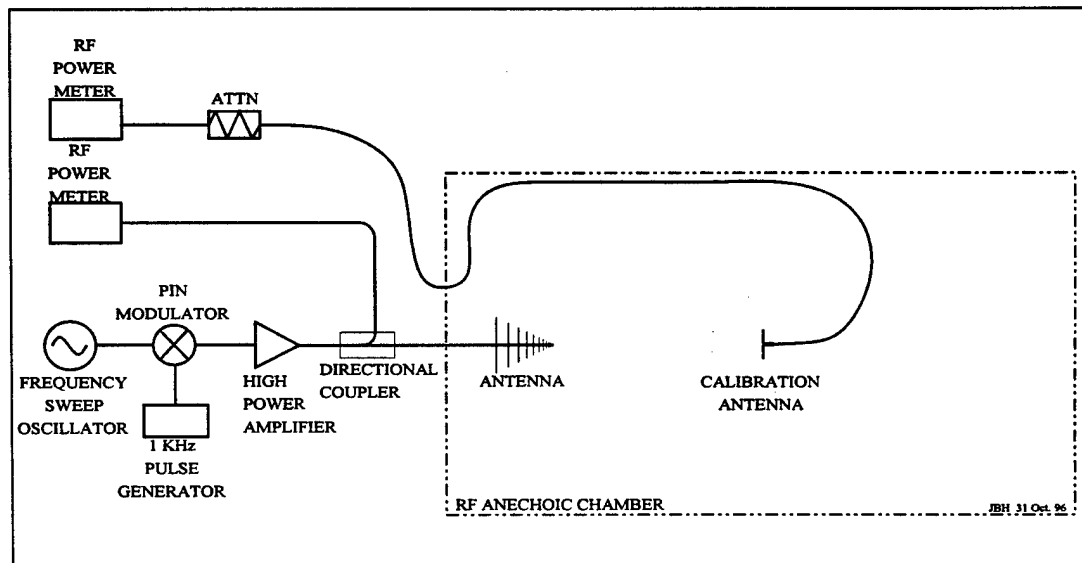


Figure 12. Narrow band chamber calibration instrumentation.

Coupling measurements were made by replacing the calibration antenna and power meter with the pseudomissile and its associated response monitor equipment. The configuration shown in figure 13 results. The remote monitoring instrumentation was previously shown in figure 5.

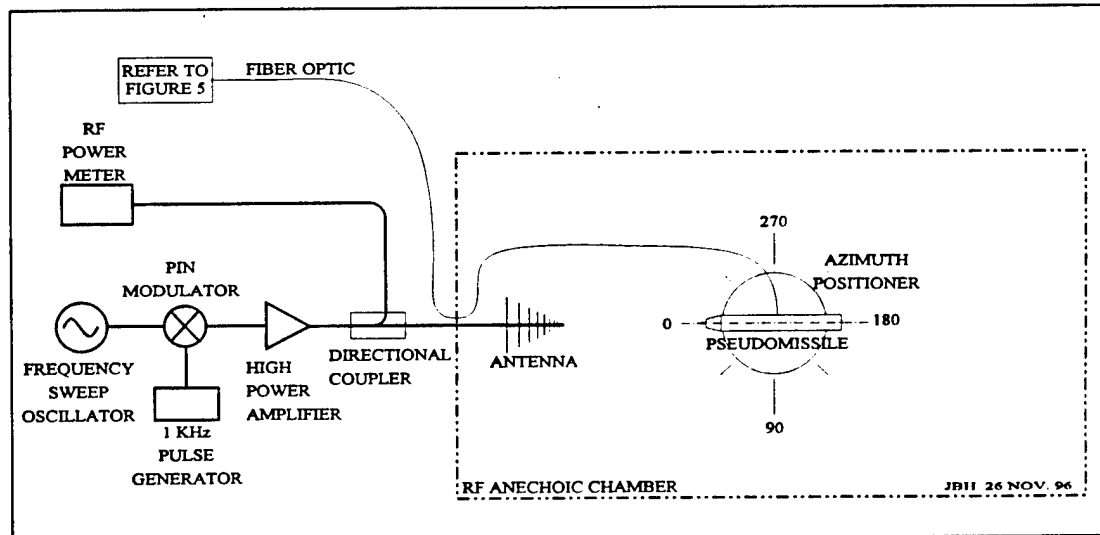


Figure 13. Narrow band chamber configuration.

4.2 Ultra-Wide Band

Ultra-wide band measurement instrumentation was configured in the I&EPD EMAF's large anechoic chamber. Figure 14 is a picture of the impulse measurement configurations for the scattered field measurements. From left to right, transverse electromagnetic (TEM) antenna with impulse source, pseudomissile on a foam column in front of the absorbing barrier, and the D-dot field sensor. The foam support column has good dielectric characteristics ($\epsilon_p \cong 1$, $\mu_p \cong 1$) for such measurements. This series of scattering measurements was restricted to the bistatic configuration shown, with the pseudomissile oriented 180° from that shown in figure 14 (nose toward the absorbing barrier). Figure 15 is a plan view block diagram depicting this configuration.

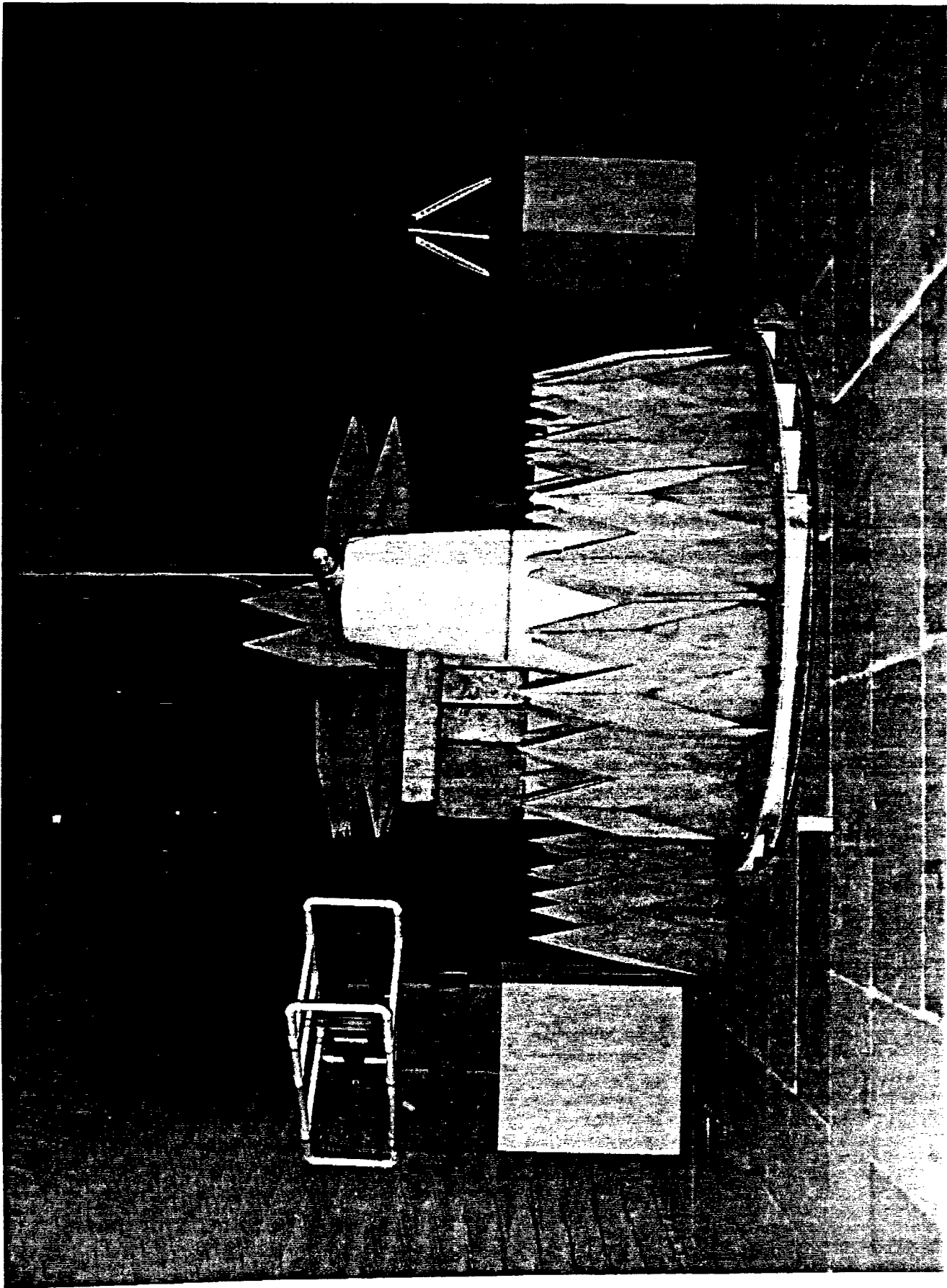


Figure 14. Impulse scattering configuration.

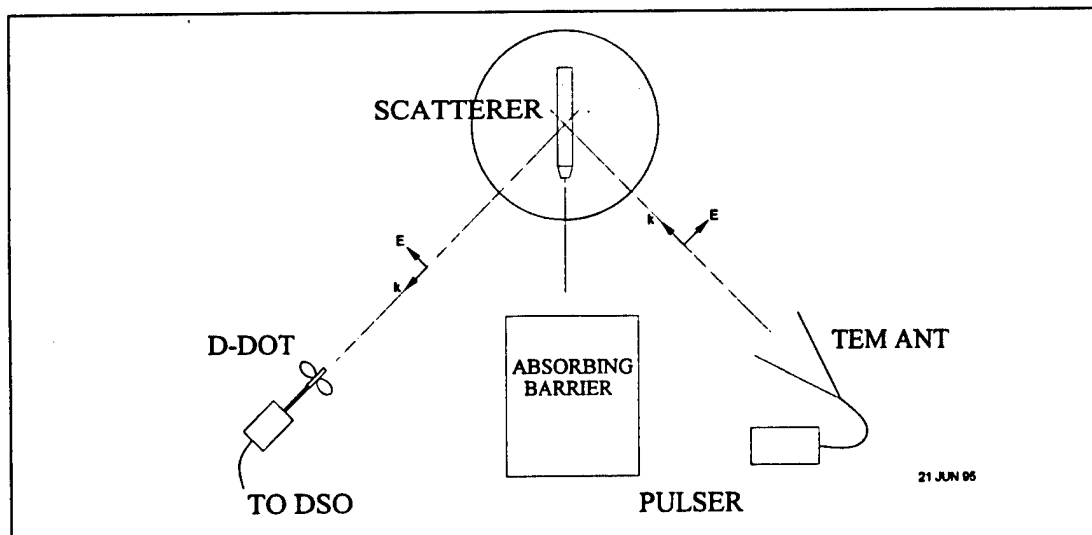


Figure 15. Wide band bistatic scatter block diagram.

The impulse approach was used as part of the in-house development program designed to reduce the amount of time presently necessary to perform EMI susceptibility assessments of U.S. Army systems. A Grant Applied Physics model HMP1 impulse source shown in figure 16 was used as the impulse source. This source provides the 4 kV pulse shown in figure 17 into a 50 Ω load with a 90 ps rise time and a maximum repetition rate of 1 kHz. The pulse shown in figure 17 is attenuated in amplitude by half due to uncompensated cable losses. This source was selected over a higher voltage source to avoid problems associated with voltage breakdown and connector arcing. A Prodyne D-dot field sensor shown in figure 18 was used for the scatter measurements. The Tektronix model 11801B digital sampling oscilloscope (DSO) with the SD-24 20 GHz time domain reflectometer (TDR) sampling head shown in figure 19 was used to record the scattered or coupled voltage waveforms.



Figure 16. HMP1 impulse generator and TEM antenna.

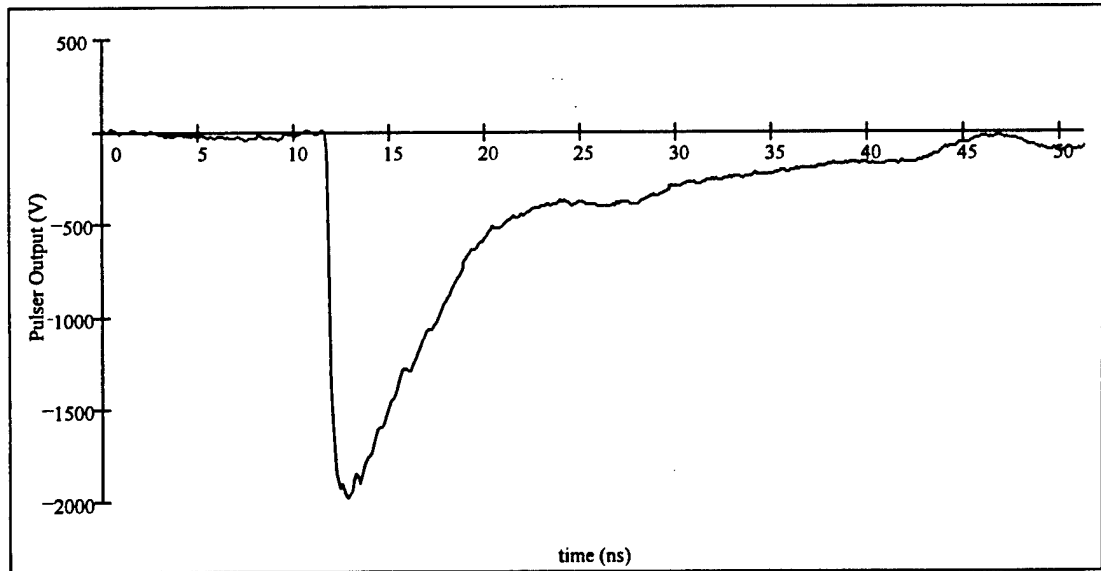


Figure 17. Signal from the HMP1 impulse generator.

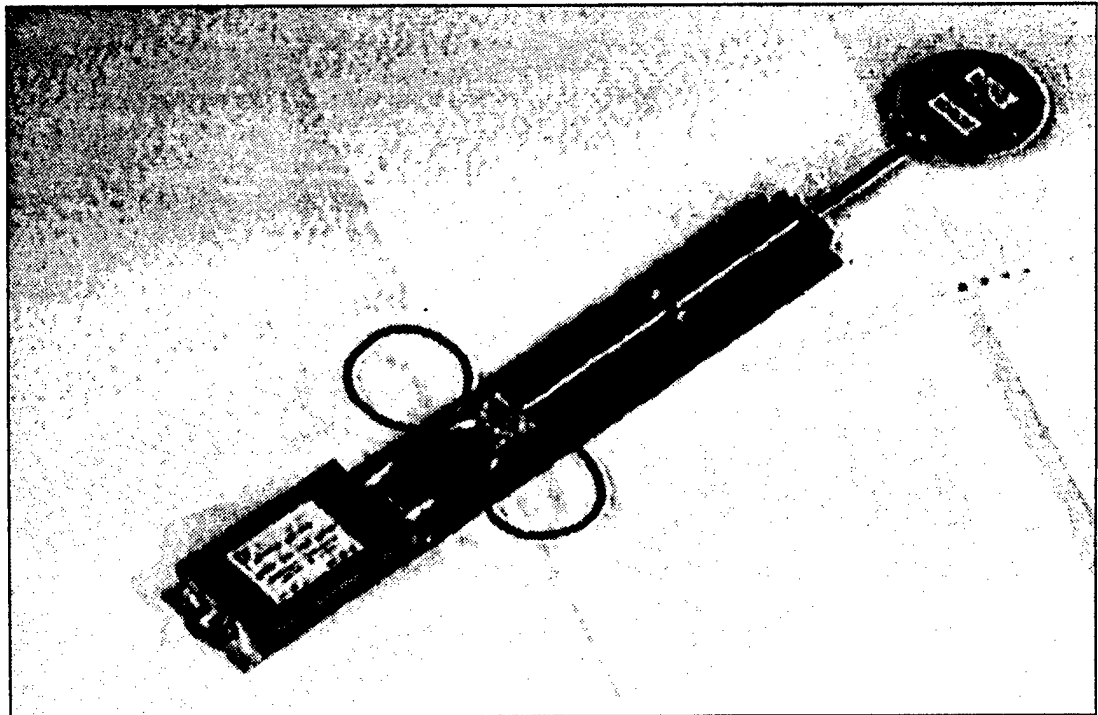


Figure 18. Prodyne D-dot field probe.

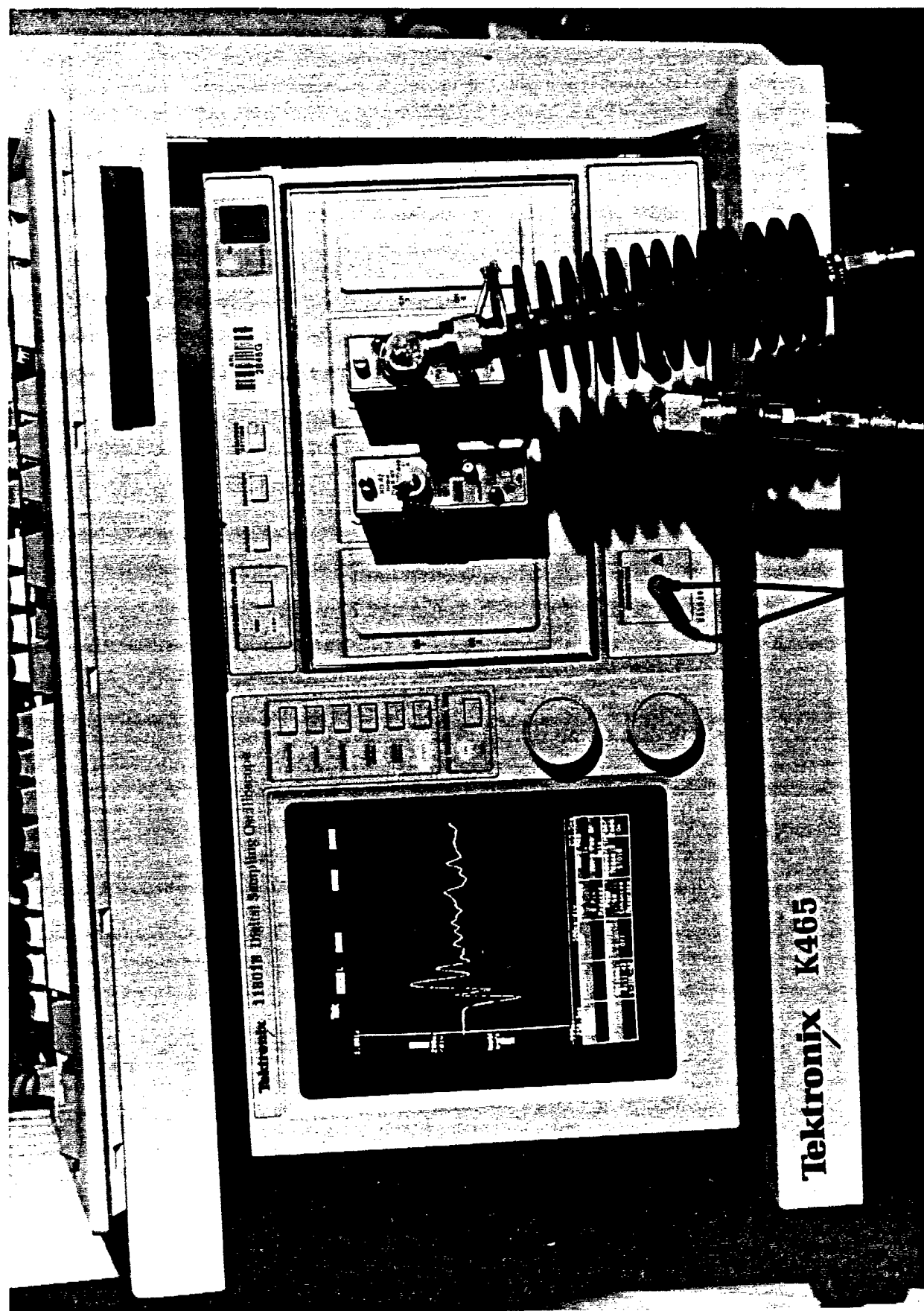


Figure 19. Digitizing oscilloscope.

Conventional ultra-wide band antennas such as log-periodics are strongly dispersive. Pulse compression postprocessing on the received waveforms was one solution. However, in order to reduce the errors associated with post-processing and imperfect data capture, the TEM antenna was designed and built. A 4-ft RG214 coaxial cable was used to transmit the impulse from the source to the TEM antenna. This cable is low-loss for signals as high as 10 GHz. The receive antenna of figure 18 was a Prodyne AD-70 D-dot differentiating electric field sensor with a Prodyne model BIB-100F balun. The specified band of operation for this sensor/balun pair was 200 kHz to 3 GHz. For scattering measurements, the D-dot sensor output was fed into a 110 ft Andrews LDF4-50A low-loss helix coaxial cable.

The received scattered waveform was digitized and displayed on the DSO. In order to increase the signal-to-noise ratio, an ensemble average of 16 waveforms was made. The averaged signal was retrieved from the DSO over its IEEE-488 data bus using an Intel 80486 based PC. The PC was equipped with a National Instruments IEEE-488 data bus interface card and LabWindows. The Automated Microwave Instrumentation (AMI) software was originally written in C by the Los Alamos National Laboratory to make high power pulse measurements using the Tektronix 7250 transient digitizer and 512 point Tektronix digitizing camera. AMI was rewritten in the LabWindows environment to suit the EMAF requirements and called BAMI, which stands for the B version of the AMI program. [7] To make full use of the equipment at the EMAF, the new program reads and processes data from the Tektronix SCD 5000 high-speed transient digitizer, the DSA-602 digital sampling analyzer, and the Tektronix model 11801B.

Fourier analysis was applied to the collected data. Wide band calibration and analysis procedures are discussed in more detail section 5.2.

5. Experiments

5.1 Narrow Band Coupling

5.1.1 Calibrations

5.1.1.1 Field Strength

Narrow band coupling calibration techniques were typical. As figure 12 shows, the pseudomissile was replaced with a standard dipole. The power density at the center of the azimuth positioner was computed using the equation

$$S = \frac{P_r}{A_{eff}} \quad (\text{W} / \text{m}^2) \quad (2)$$

where

P_r = the received power (W)

A_{eff} = the receive sensor effective area (m^2).

The effective area of the receive antenna is

$$A_{eff} = \frac{G_r \cdot \lambda^2}{4\pi} \quad (3)$$

where

G_r = receive antenna gain (1.64 for an efficient $\lambda / 2$ dipole)

λ = wavelength of the radiation being measured (m).

This calibration was performed in 10 MHz increments across the 100 to 1000 MHz band. Calibrations in the 1 to 3 GHz band were made using the standard gain horn antennas.

Power losses due to attenuators and cables were measured with an average power meter and a calibrated signal source or with a Wiltron model 560A scalar network analyzer. The EMAF chamber calibration is discussed in detail in *Data Acquisition Processing Reduction (DAPR) User's Manual*. [8]

5.1.1.2 Telemetry

A thermal drift error was discovered to occur over the measurement period. The TM became less responsive as it became warm during operation. The TM

thermal drift over time was measured and is plotted in figure 20. The TM thermal drift error affected the coupled response level. Once this error was discovered it was kept within ± 1.5 dBV of the -50 dBV level defined as the response threshold.

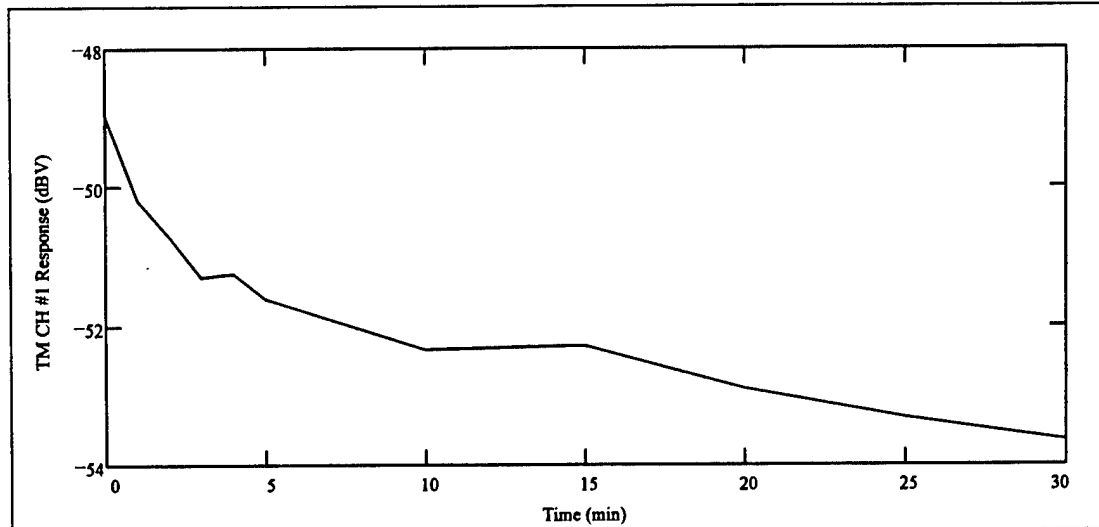


Figure 20. Thermal drift of the measured response versus time.

5.1.1.3 Diode

The diode input power versus output voltage transfer function was measured in the laboratory with the setup of figure 21. A threshold response level of -50 dBV, as measured on the HP 3561A dynamic signal analyzer, was defined for the 1 kHz fundamental spectral line of modulated RF detected by the system (see section 5.1.2). Figure 22 shows the diode calibration response. This calibration response was flat to within ± 1 dB in RF power from the 100 MHz to 3 GHz band for a -50 dBV threshold response. Thermal drift error was not allowed to vary more than 1 dB over a particular sequence of calibration measurements. The calibration sequence consisted of power on for two minutes and collect response data, then power off to cool the TM for five minutes. This power on/off cycle was repeated through the frequency sweep calibration measurements.

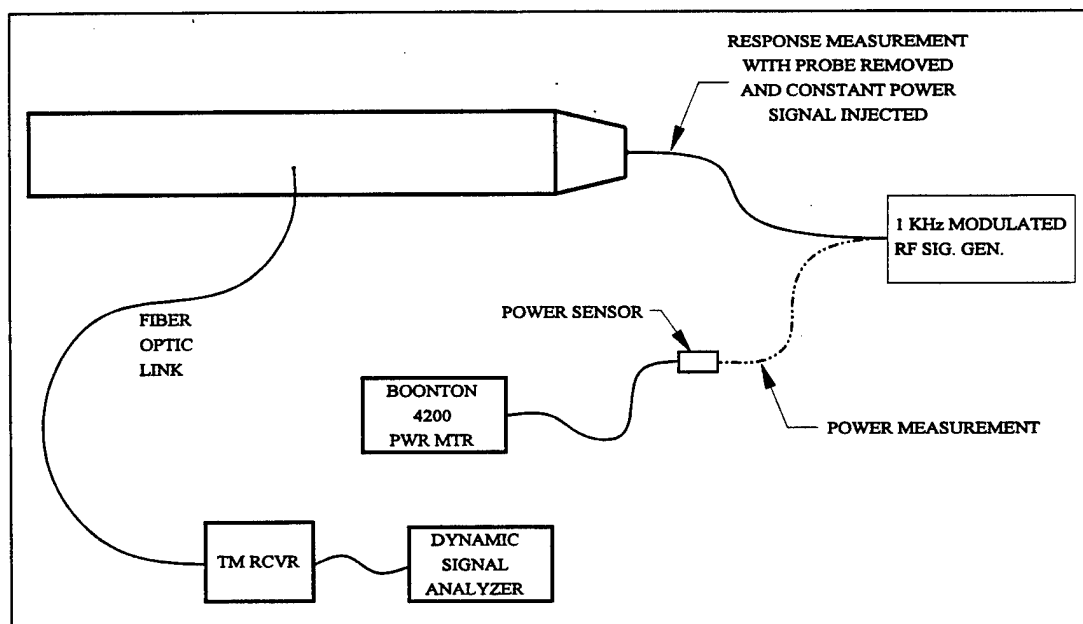


Figure 21. Diode calibration setup.

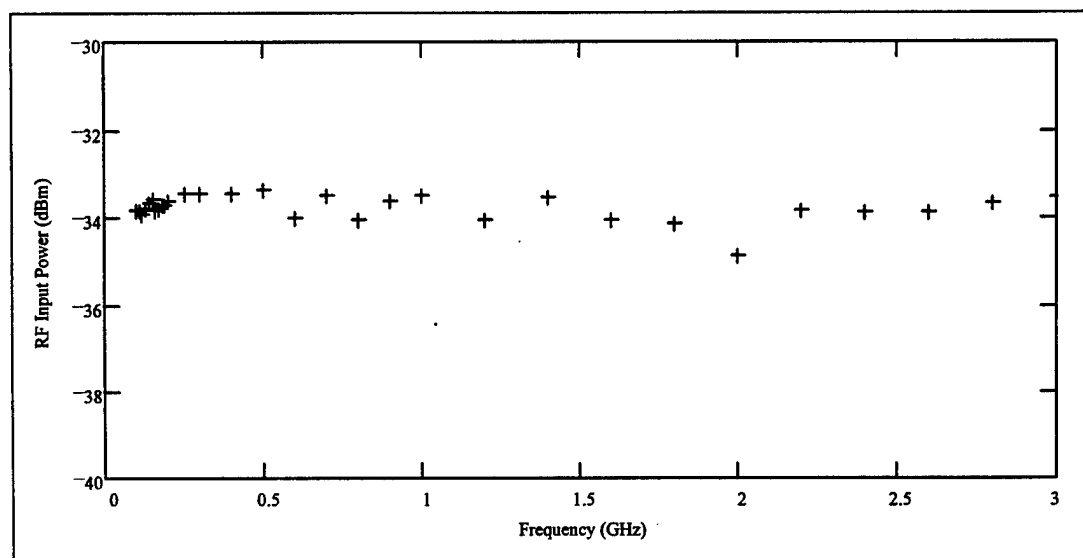


Figure 22. Diode 2 input power versus frequency for a -50 dBV response on TM channel 1.

5.1.2 Measurements

Electronic systems tend to have a significant DC bias that reduces the dynamic range of its response to a simple continuous wave (CW) RF coupled signal. To improve the dynamic range of response, the incident RF signal was pulse modulated with a 1000 Hz square wave. The system response was measured on the HP3561A dynamic signal analyzer with the configuration shown in figure 5.

A susceptibility response level of -50 dBV was defined, as discussed in the previous section. The RF power level was adjusted until this level was reached. The frequency was incremented, and the power level for -50 dBV response was recorded. This was repeated in 10 MHz steps below 1 GHz and every 50 MHz above 1 GHz. The resulting power density versus frequency plot is given in figure 23. Note in this plot the distinct valleys exhibited by the data below 1 GHz. These are resonances which result from the excitation of the body modes of region I shown in figure 6. There is an inverse relation between the power density required to induce a system response and the system's susceptibility. In order to clarify these resonances, figure 23 is replotted in the form of a normalized susceptibility profile in figure 24. In figure 24, the resonances now correspond to the peaks in the data. Comparison with the scatter data will be discussed in section 6. A particularly interesting feature of the narrow band coupling data was the strong peak at 1.3 to 1.5 GHz. This frequency corresponds to the $\lambda/2$ resonant frequency of the small probe and its image in the circular frustum ground plane cap as discussed in section 3.

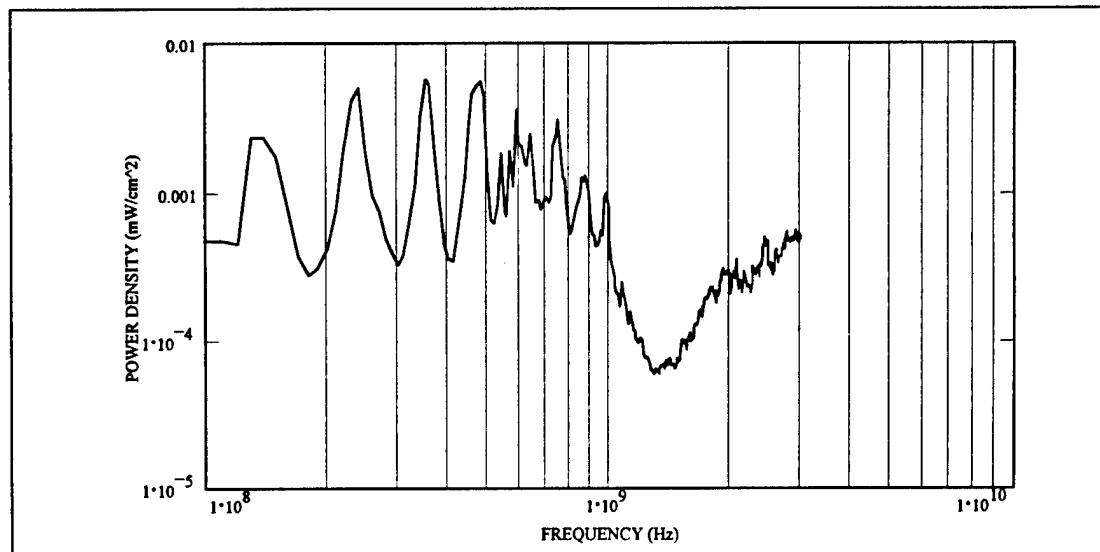


Figure 23. Power density required to induce a -50 dBV TM channel 1 response.

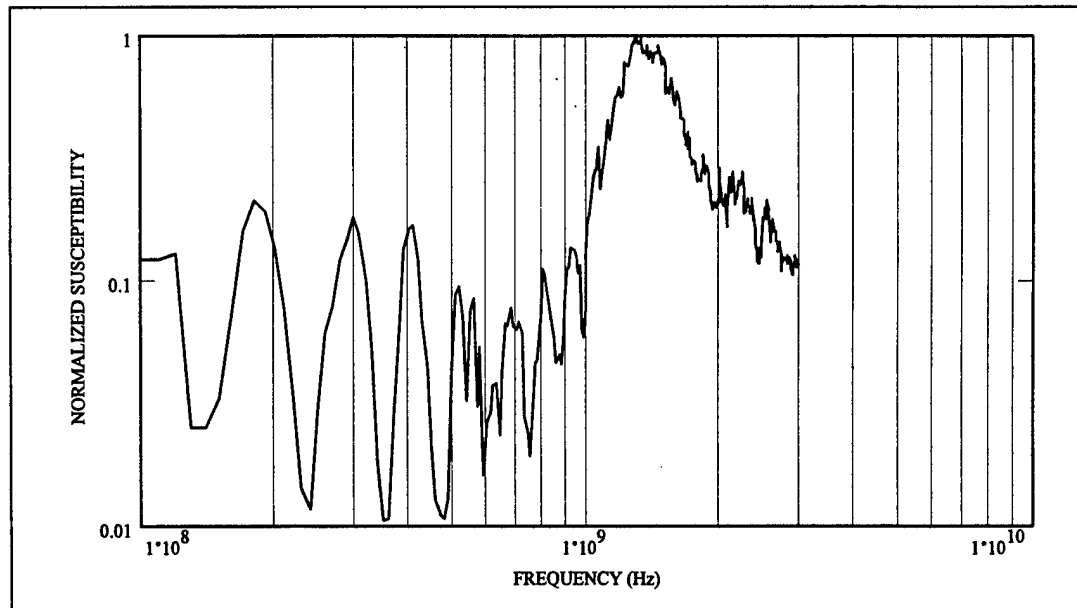


Figure 24. Normalized susceptibility of the pseudomissile.

The dominant resonant peak observed in figure 24 was not well defined due to multiple interactions, such as from the finite ground plane and the higher order body modes.

5.2 Wide Band Scattering

Data collected with the BAMF software was saved in two column (time and voltage) American Standard Code for Information Interchange (ASCII) format. This format was chosen for the signal processing prototype development since ASCII can be read by most of the processing programs available at the EMAP. MathCAD is used for quick development of data processing algorithms. The application of these algorithms is shown in sections 5.2.1 and 5.2.2.

5.2.1 Calibrations

A calibration procedure was required before scatter measurements could be made. The first step was to measure the radiated short-pulse field by placing a D-dot field sensor in the center of the measurement volume. Then the scatterer was placed in the measurement volume, and the D-dot field sensor was placed in its bistatic configuration for the scatter measurements to be made without the pseudomissile present. A background measurement was made. The pseudomissile was placed in the measurement volume, and the scatter response plus background was measured.

5.2.1.1 Coaxial Cables

Compensation for coaxial cable distortion was unnecessary to the algorithm since the same cables were used for measuring both scattered and incident waveforms. Division of the scattered waveform with respect to the incident waveform frequency spectra eliminated the dispersive and high frequency roll-off loss effects of the cables.

5.2.1.2 EM Field

The Prodyne D-dot sensor of figure 18 was used to make all impulse scattered field measurements. The sensor output voltage ($V_{out}(t)$) is proportional to the product of the sensor impedance ($Z_s=50\Omega$), effective area ($A_{eff} = 10^{-3} \text{ m}^2$), and time rate of change of the electric flux density ($d\mathbf{D}/dt$). That is

$$V_{out}(t) = Z_s A_{eff} \frac{d\mathbf{D}^{inc}}{dt} \quad (\text{Volts}) \quad (4)$$

The incident electric field (\mathbf{E}^{inc}) is computed by integrating $V_{out}(t)$ with respect to time and dividing by the product of the dielectric constant of free space (ϵ_0), sensor impedance (Z_s), and the effective area (A_{eff}). So the electric field is then

$$\mathbf{E} = \frac{1}{\epsilon} \int \left[\frac{d\mathbf{D}}{dt} \right] dt \quad (\text{V m}^{-1}) \quad (5)$$

$$\begin{aligned} \mathbf{E}^{inc} &= \frac{1}{\epsilon_0} \int \frac{V_{out}(t)}{Z_s A_{eff}} \hat{\mathbf{p}} dt \\ &= \frac{1}{\epsilon_0 Z_s A_{eff}} \int V_{out}(t) \hat{\mathbf{p}} dt \end{aligned} \quad (\text{V m}^{-1}). \quad (6)$$

where \mathbf{p} is the electric field polarization vector. For these scattering measurements, the propagation vector of the electric field was oriented 45° with respect to the pseudomissile body axis. The electric field was copolar with the body axis. The polarization axis of the D-dot field probe was polarized with a 90° rotation with respect to the incident electric field. This is shown in figure 15. Appendix A shows the MathCAD implementation of this equation for computation of the incident field.

EM field baseline references were made for both the corrected incident field shown in figure 25 and the background signal shown in figure 26. Measurement of the incident and background signals is discussed with more detail in section 5.2.2. These signals allowed the necessary calibration corrections to be made. The incident field must be known in order to compute the exterior-to-interior transfer function as well as the bistatic scattering transfer function with respect to angle of incidence. Although these measurements were performed in an anechoic chamber, the incident impulse field caused low-frequency cable oscillations to appear in the measured waveforms. These cable oscillations, along with antenna cross talk, stray scatter signals, and mutual interactions, were measured to be subtracted element by element from the scattered signals. Appendix B implements this subtraction. An unfortunate side effect of excessively large background signals was the reduction in the dynamic range of the signal data.

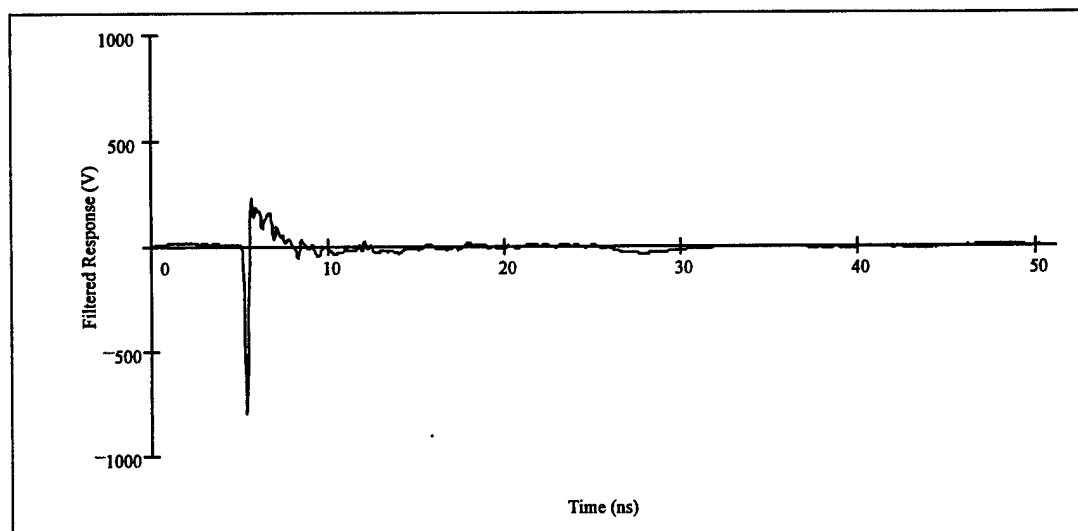


Figure 25. Incident field.

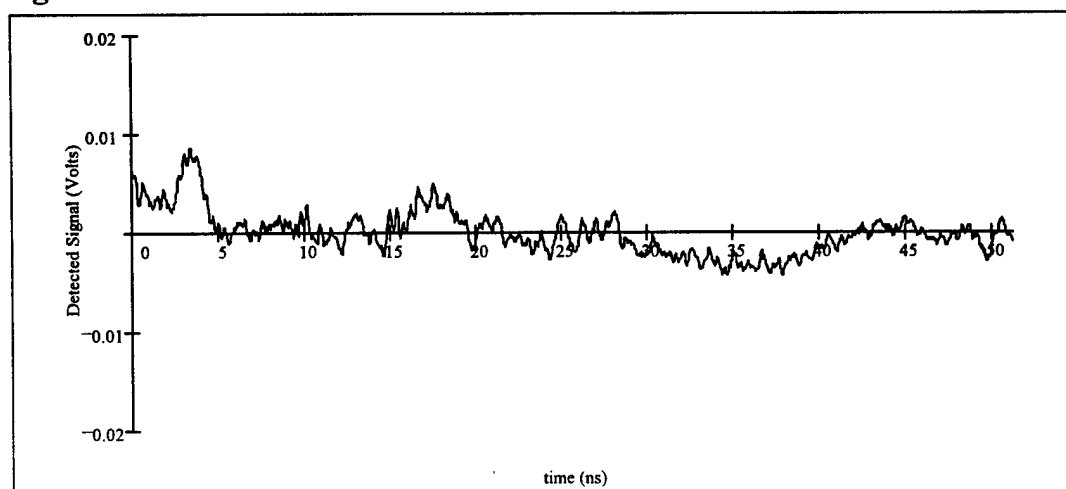


Figure 26. Background signal.

The incident waveform and the input pulse contains all the necessary information about the effect of the TEM antenna on the pulse spectrum. No additional characterization was necessary.

5.2.2 *Anechoic Chamber Scattering Measurements*

Bistatic impulse scattering measurements were conducted on the pseudomissile in the EMAF's large anechoic chamber (figure 14). The graphic diagram for the setup of this bistatic scatter experiment is shown in figure 15. The bistatic angle $\beta = 90^\circ$ was selected for two reasons. One reason was that a separation between the transmit and receive antennas allowed the placement of a large RF-absorbing barrier between the two antennas to reduce the amount of cross talk. The second reason was that significant reradiated energy from body modes was expected to be observable for the given configuration. These late-time resonant scatter modes were expected to provide the desired information about the frequencies at which a coupled signal may induce the strongest system response. The scatter response as used in this paper assumes linearity.

The incident waveform of figure 25 was measured by replacing the pseudomissile with the D-dot field sensor and applying the appropriate integration and scaling for the specific sensor. The specified effective area of the Prodyne D-dot sensor used was 10^{-3} m^2 . Correction for both cable loss and differentiation from the D-dot sensor was not necessary due to normalization of the scattered field with respect to the incident field. However, for the sake of physical meaning, the fields were integrated and the cable loss was compensated for in appendix A. Since integration of digitally sampled data sets results in significant error for these transient waveforms, the signal was highpass filtered with a second-order Chebyshev filter having a 100 MHz cutoff frequency and a 0.5 dB ripple. The 100 MHz cutoff was defined due to the lowest effective frequency of the EMAF large anechoic chamber as well as the effective lower frequency limit measured for the antenna. The second-order Chebyshev filter was selected over a higher order filter so as not to eliminate too much of the low frequency energy (since some of this energy was not an artifact). The 0.5 dB passband ripple was chosen to provide only a small amplitude distortion to the amplitude spectrum across the passband. The degree and type of digital filtering was chosen such that the signal appeared nearly causal. The incident field strength was computed as 1,100 V/m with a 10 to 90 percent rise time of $\sim 200 \text{ ps}$. The spectral energy of this impulse extended to approximately 7.5 GHz.

The scattered waveform before the subtraction of the background waveform is shown in figure 27. Subtracting the background signal of figure 26 leaves the scatter waveform of figure 28. A small ripple occurs in the scattered waveform from 46 ns to the end of the waveform record in figure 29. This waveform appeared to be the result of scattering from an object other than the pseudomissile. The scatter record was set to zero from 46 to 51.15 ns in the integrated waveform of figure 29. Applying the integration and filtering used for computing the incident impulse signal, and setting the last 5.15 ns to zero, results in the waveform of figure 29. Normalization was then performed with respect to the incident waveform using a singularity filter ($K = 0.15$) to reduce the effects of noise at the higher frequencies. In a similar fashion to the Wiener filter, the smoothing constant K is inversely related to the signal-to-noise levels. It was found that a constant value of $K = 0.15$ introduced minor amplitude shifts but significantly reduced the high frequency noise in the bistatic transfer function. Appendix C shows this process. The resulting deconvolution of the scattered waveform with respect to the incident waveform yielded the impulse scatter response of the pseudomissile shown in figure 30. Residual artifacts are evident in the scatter response. The first sharp doublet response occurs at ~ 6.5 ns into the record. A response begins prior to this first (early-time) specular flash. This cannot occur for a causal system. This is an artifact and is believed to have only a small influence on the modal frequencies culled from this data. The magnitude versus frequency transfer function of the pseudomissile is shown in figure 31¹. The observed frequency peaks occur in the scattered spectrum at <100 , 196, 303, 391, and 508 MHz. These correspond to the first five body modes for the pseudomissile. The frequency peaks that occur above these first modes appear significant, but as will be discussed further in section 6, they do not appear to be the dominant cause of susceptibility.

¹ Phase is not shown because all phase information of the carrier is lost in the detection process and would be meaningless for this analysis. This is not to say phase is unimportant.

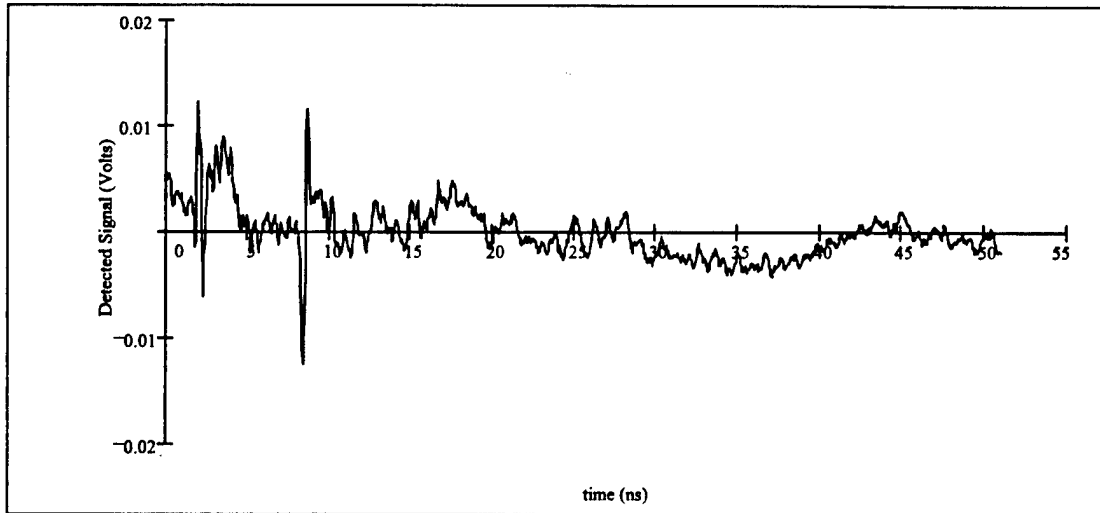


Figure 27. Background signal with pseudomissile scatterer.

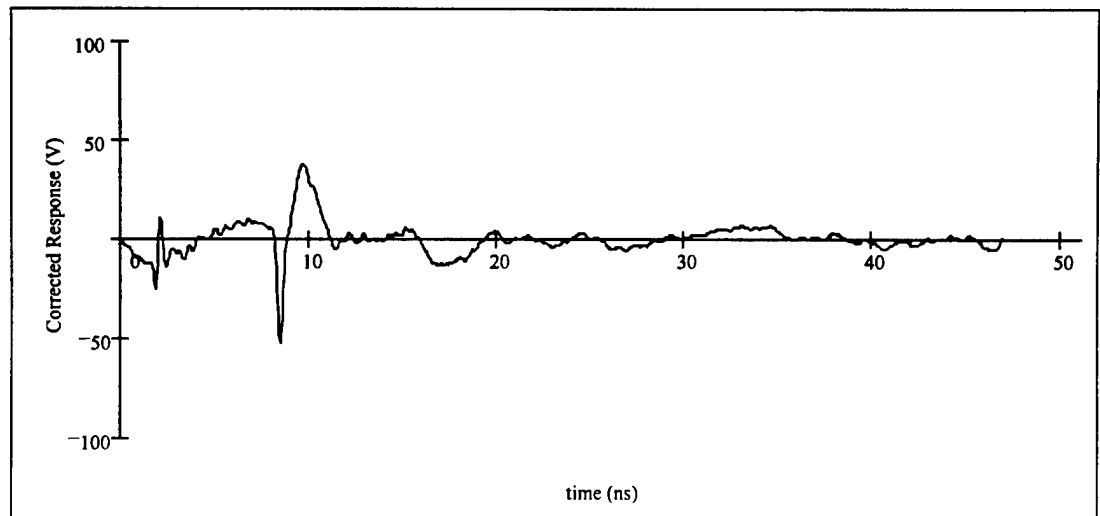
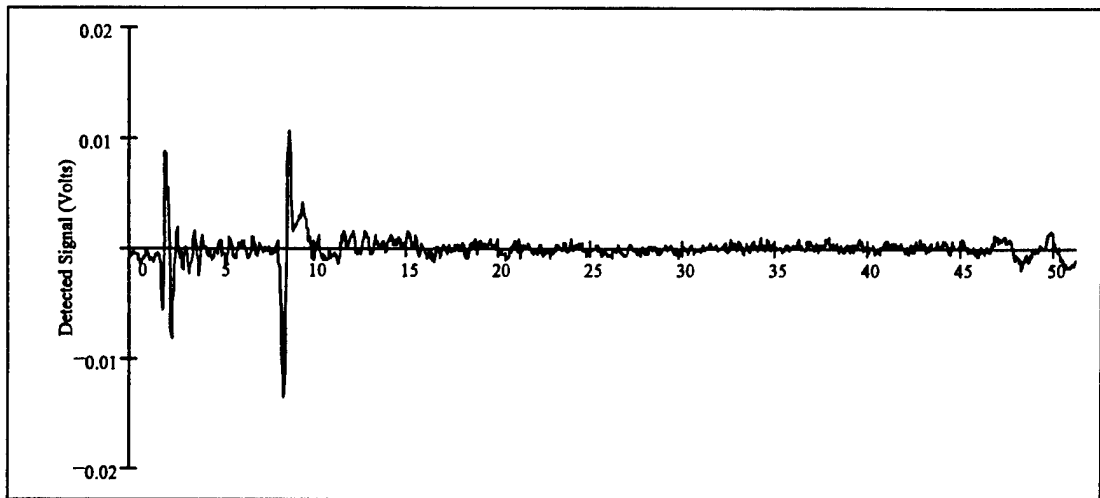


Figure 28. Scatter response of pseudomissile.

Figure 29. Integrated scatter response.

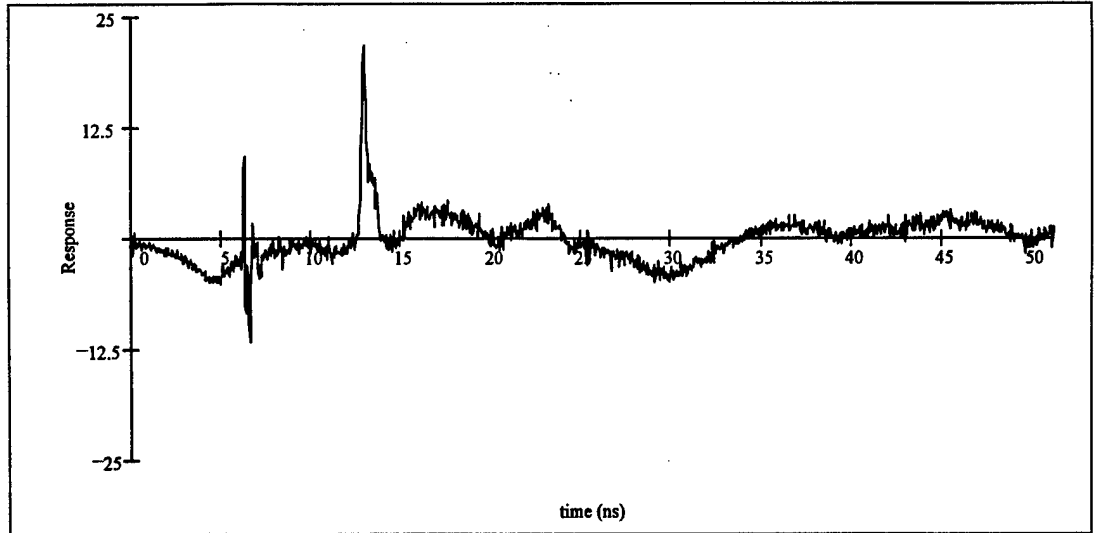


Figure 30. Pseudomissile impulse scatter response ($K = 0.15$).

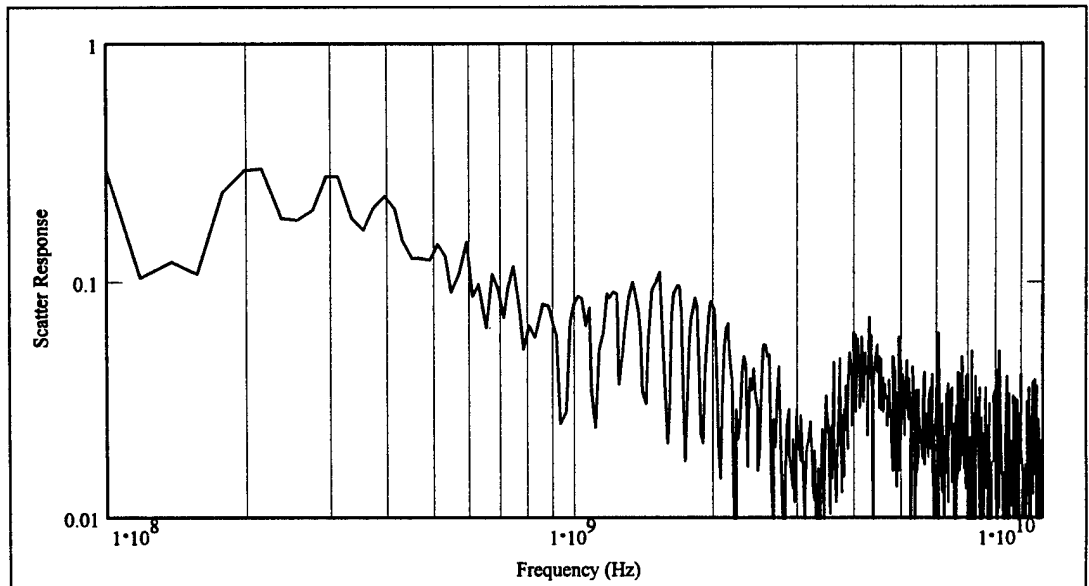


Figure 31. Normalized bistatic scatter transfer function ($K = 0.15$).

The deconvolution operation was performed by transforming the time signals into the frequency domain and then dividing the scattered signal by the incident signal. Since the signal becomes noisy as the frequency increases, the transfer function also becomes increasingly unstable. As previously mentioned, the effects of this noise were reduced by applying a noise filter with a constant coefficient of $K = 0.15$, as indicated in figures 30 and 31. A small but insignificant distortion was introduced to the resulting signal. The most notable effect of the noise filter used for this purpose was the marked reduction of the severe, artificial, high-frequency noise components. These components occur

as a result of the near singularities when the scattered incident field is divided by a noisy incident field.

The procedure developed to compute the system's scatter transfer function is summarized in figure 32. This algorithm is essentially the same as that given by Morgan. [9]

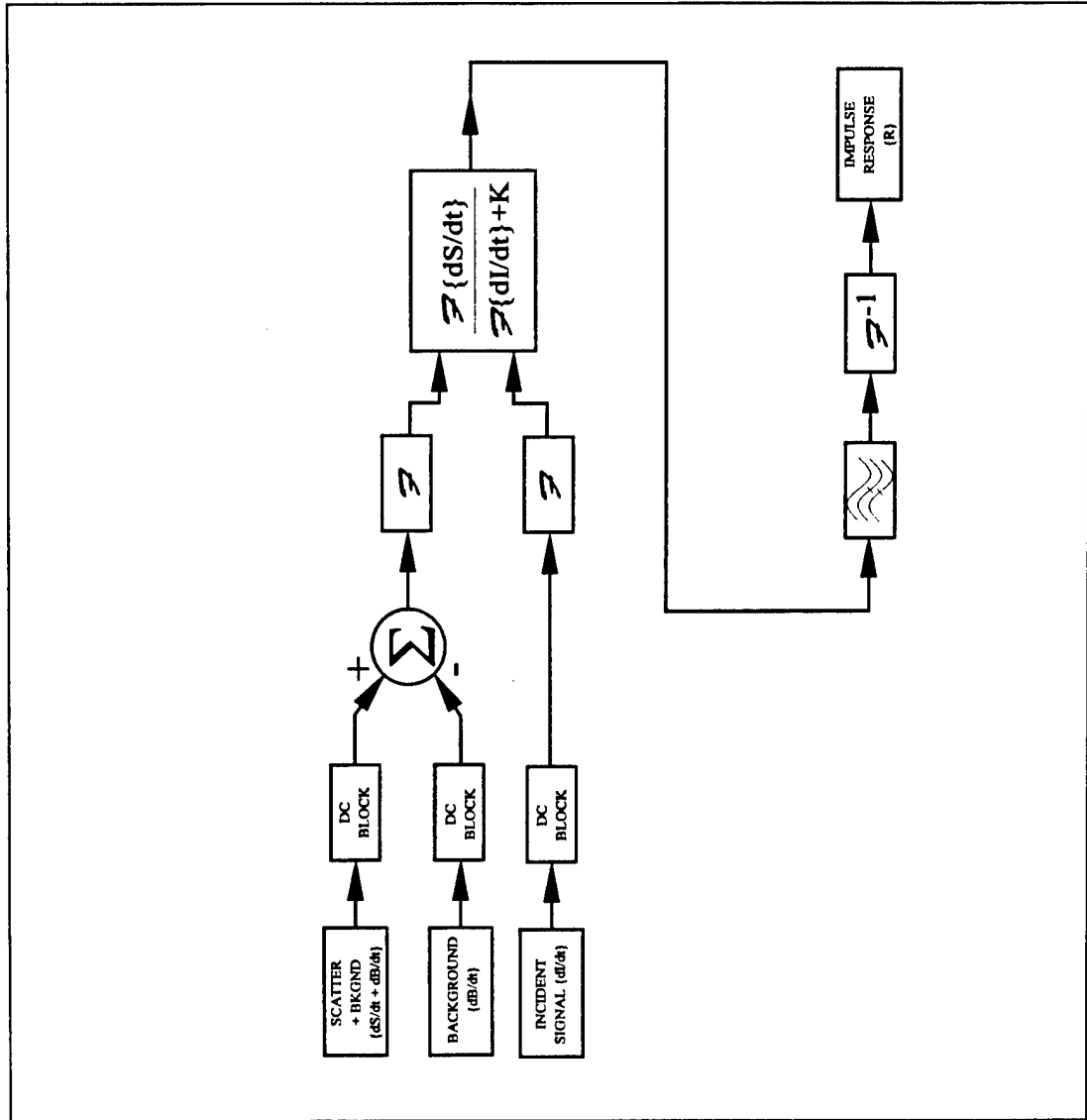


Figure 32. Impulse response computation algorithm.

5.2.3 Ground Plane Scattering Measurements

In the measurement data presented so far, it is not possible to identify the most susceptible frequency observed at 1.3 to 1.5 GHz for the pseudomissile. In order to extract the susceptibility frequency, data collected on the ground plane was carefully analyzed.

Prior to the development of the U.S. scatter capability at the EMAF, a series of scatter measurements was conducted above a ground plane in August 1994. A detailed time-frequency, energy, and bitime self-correlation analysis of pseudomissile scatter data was made by Dr. Eric Walton of Ohio State University. [2] Data used for a portion of the analysis performed by Dr. Walton is the focus of this section. Figure 33 shows the configuration used for the ground plane scatter measurements.

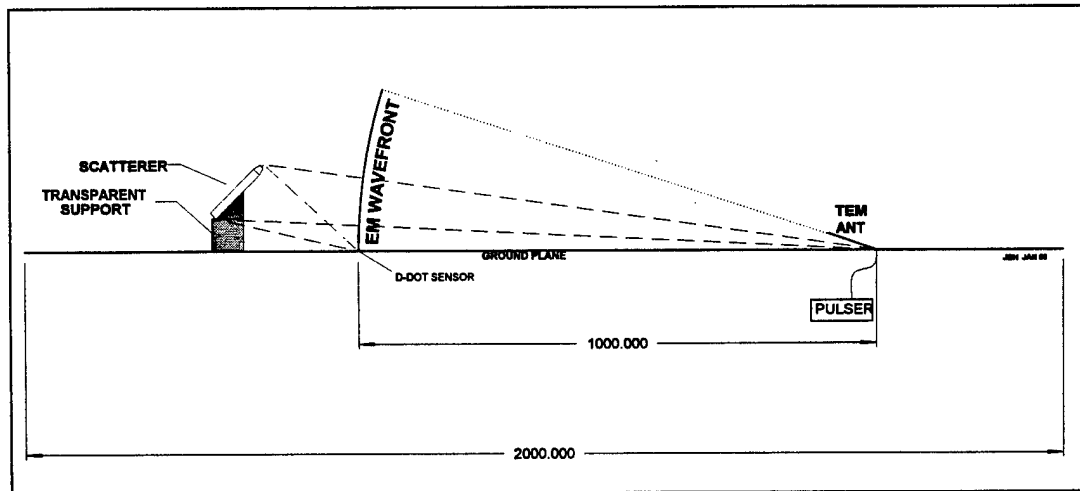


Figure 33. Ground plane scatter geometry.

A series of measurements was performed with both a variation of probe loading as well as missile orientation. As with the experiments presented in the previous sections, the dominant scattering modes are from the missile body. A technique for isolating the probe scatter is presented and analyzed here. The pseudomissile was configured as shown in figure 33 with the probe wire present. This configuration best matches that used in the EMAF large anechoic chamber. Detection of the scattered signal produced figure 34.

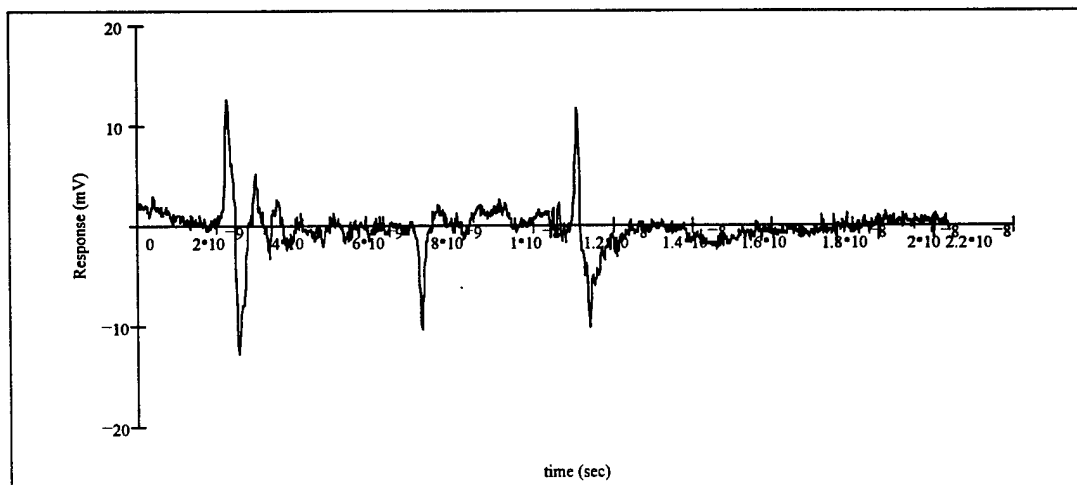


Figure 34. Scatter signal with probe present.

The probe on the forward tip of the pseudomissile was then removed and the measurements repeated, resulting in figure 35. Notice the decrease in the oscillation response after the first specular flash, located ~ 3 to 5 ns into the record when compared to figure 34.

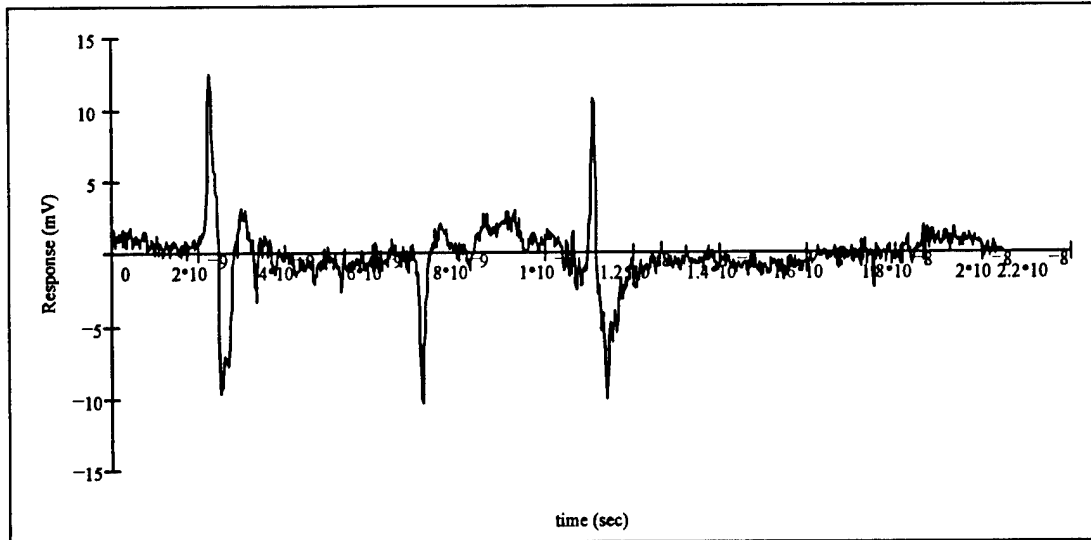


Figure 35. Scatter signal without probe present.

The difference between the signal present in figures 34 and 35 is shown in figure 36.

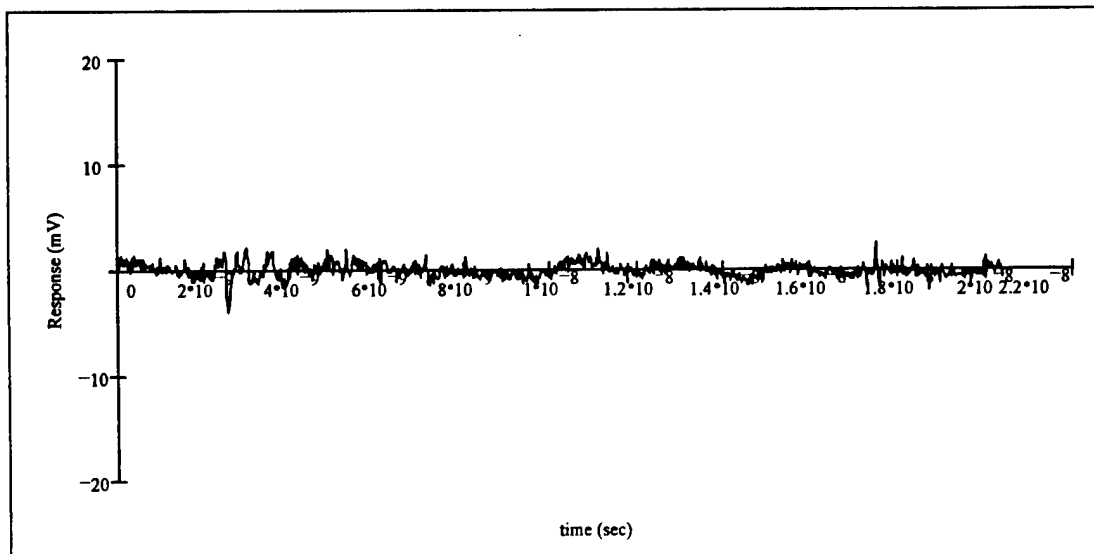


Figure 36. Difference signal between figures 34 and 35.

Since it was known that the probe responded within the ~ 2 to 7 ns window, a rectangular window was applied to figure 36, which isolated the probe region's (region II) response as shown in figure 37.

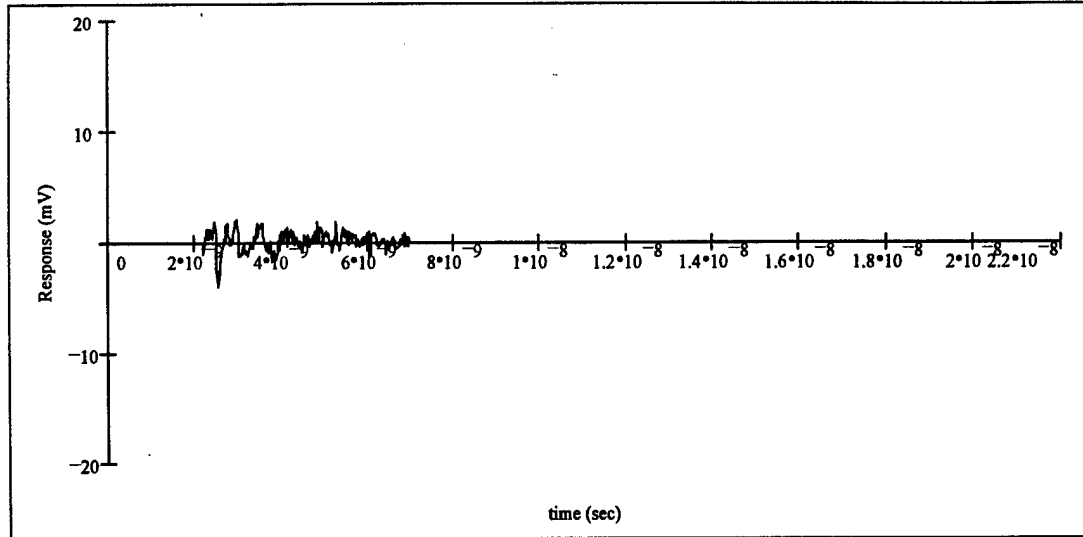


Figure 37. Rectangular "short-time" windowed waveform.

Without windowing, residual body modes dominate the response, deemphasizing the desired region II response containing the probe resonances. The "short-time" windowed signal was transformed into the frequency domain, resulting in the frequency spectrum shown in figure 38 (with the distinctive response shown at 1.54 GHz). No additional processing such as integration, cable compensation, or noise filtering was applied.

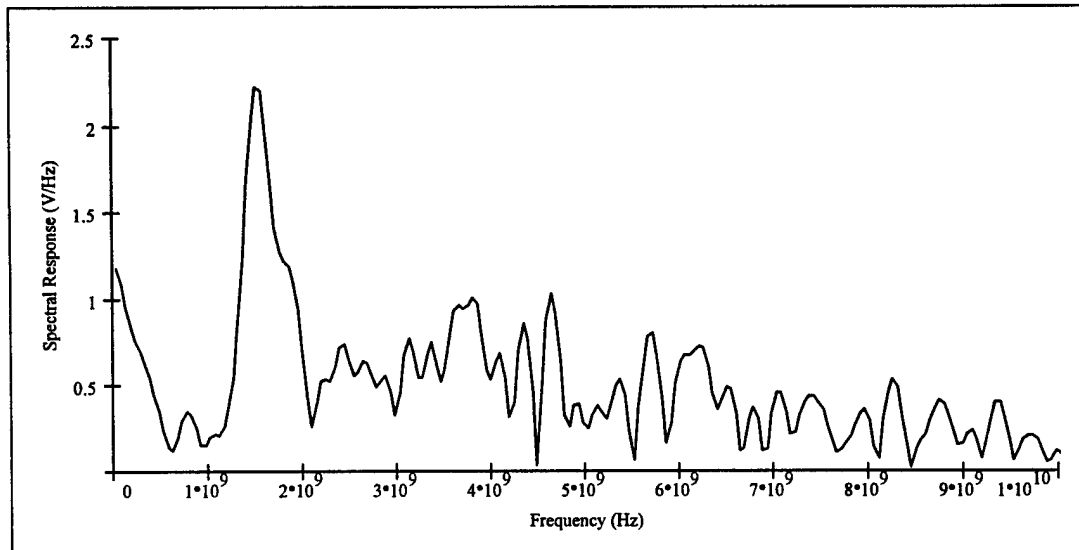


Figure 38. Fourier transform of the windowed difference waveform.

6. Comparison of Results

Since the coupled signal defines the system's susceptibility, the narrow band coupling data was considered to be the reference to which all other data was compared.

The probe at the tip of the missile behaves as a thin monopole above a truncated circular ground (region II). The axial ratio of the probe was ~ 65 . The body/frustum combination behaves as a thick dipole with an axial ratio of ~ 8.5 . An estimate of the resonant frequencies for these two missile regions was made using both simplistic $n\lambda/2$ approximations and thick wire computations. Thin wire and thick wire modes are derived from the MSFP code developed using the singularity expansion method (SEM). In addition to these simple computations, a wireframe model was developed for NEC 2, and a frequency sweep analysis was performed to 2 GHz. The mesh size was approximately $\lambda/10$ at 1 GHz and dropped to approximately $\lambda/5$ at 2 GHz (the upper bound of the frequency sweep). The Clemson code was not available to perform these same computations.

The simple "back of the envelope" computation yielded approximate dipole resonant modes of the missile body and the probe. These frequencies are:

$n\lambda/2$ Body modes

f = 112.50 MHz

f = 225.00 MHz

f = 338.00 MHz

f = 450.00 MHz

$n\lambda/2$ Probe modes

f = 1.46 GHz

f = 2.91 GHz

Comparing these frequencies with those measured shows that the calculated body modes are all significantly higher in frequency than the measured body modes. This was because parasitic loading was unaccounted for in this simple calculation. The probe modes were computed to occur at 1.46 and 2.91 GHz. The first probe mode corresponds with the maximum susceptibility seen in the 1.30 to 1.50 GHz band observed for the pseudomissile. The second probe mode was not observed in the coupling data. The body modes computed in this manner were useless for establishing coupling frequencies.

The MSFP was applied to each of the two cylinders. One set of input parameters corresponded to the dimensions of the pseudomissile body and the second corresponded to the parameters of the wire probe and its ideal image perpendicular to an infinite ground plane. The results of this program correspond very well with the measured data. These results most closely corresponded with the coupled measurements. These results are compared in table 4.

Table 4. Pseudomissile resonant frequencies

Mode	$n_{\lambda}/2$ calculated	SEM calculated	NEC 2 computed	Impulse scattered	Coupling measured
Body modes (MHz)					
1	112.50	88.50	90	<100*	<100*
2	225.00	190.59	190	196	183
3	337.50	295.75	280	303	300
4	450.00	402.62	380	391	404
5	562.50	510.68	560	508	519
Probe modes (MHz)					
1	1460	1313.33	not avail.	1540	1300-1500
2	2910	2722.39	not avail.	none	none

* lowest frequency measured or displayed.

The objective of this paper is to determine whether scattered fields can be used to predict coupled fields. The scatter signature of the pseudomissile was computed from the impulse scatter data collected for what was considered an optimum experimental configuration. This signature revealed a large number of peaks resulting from body resonances, as seen in figure 31. These signals were compared to the coupled signals. It was clear that the first four or five body modes that appear in the scatter data also appeared in the coupling data. However, it was tempting to interpret all of the modes observed in the scatter data as significant. The physical reason that the higher modes are not an indicator to efficient coupling is the sharp impedance discontinuity of region II with respect to the missile body. The probe's fundamental dipole mode dominates the susceptibility of the pseudomissile since there is a better impedance match about the probe/detector junction at the base of the probe. Such mismatches would not necessarily be so obvious on a real system.

Scattering measurements were made on the ground plane, which allowed the isolation of the scatter response due to scatter region II. The configuration of the experiment was not ideal. However, a fundamental resonance of 1.54 GHz was detected in this scatter waveform. To enhance this specific response, a rectangular window was placed over the probe location. The transform of this response was 227 MHz higher in frequency than expected from the

probe as predicted by MSFP. The exact cause of this is unknown. However, the diameter of the frustum cap is 1.65 times the length of the probe. Modes of the end cap may be interacting with the probe modes. This may explain why no second probe mode resonance is measured. In order to make an "infinite" ground plane approximation, the extent of the plane should be $\sim 10\lambda$ from the radiator to the edge. Mutual interactions between local scatterers will be more difficult to analyze in complex systems.

A graphical comparison between the scattered and coupled data is made in figures 39 through 41. The resonant peaks that result from these measurements are also tabulated in table 4. A sampling error is present since the sampling resolution of the collected narrow band data and the fast Fourier transform (FFT) of the impulse scatter data are not identical. Table 5 shows that the errors associated with each of the analysis methods used. These errors are meaningless without recasting them in the form of percentage bandwidth error:

$$\%BW_{err} = \frac{2|\Delta f_c|}{BW_{n-n}} \quad (7)$$

where

Δf_c = the predicted and measured modal frequency difference (table 5),
and
 BW_{n-n} = the null-to-null bandwidth of the measured modes.

Table 6 is a compilation of the percent bandwidth errors.

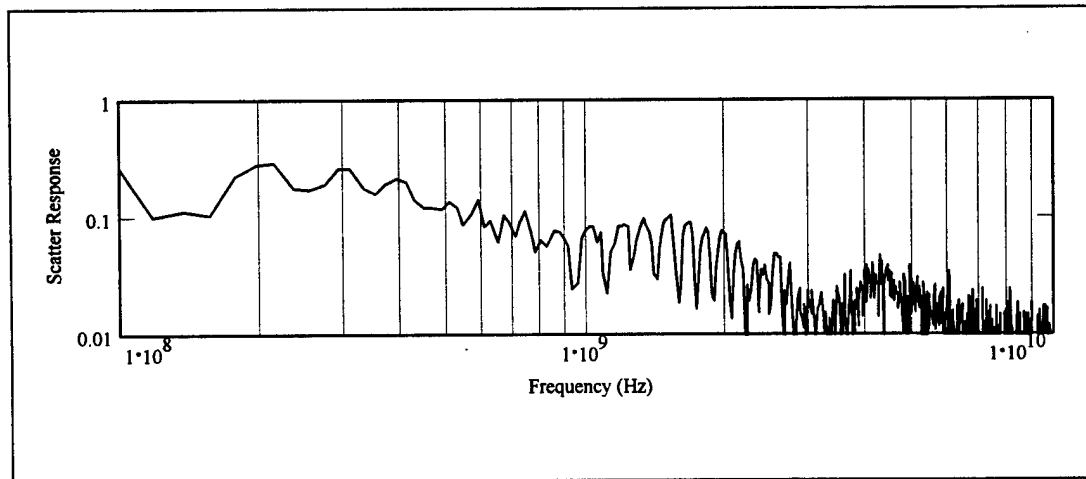


Figure 39. Scatter response (same as figure 31).

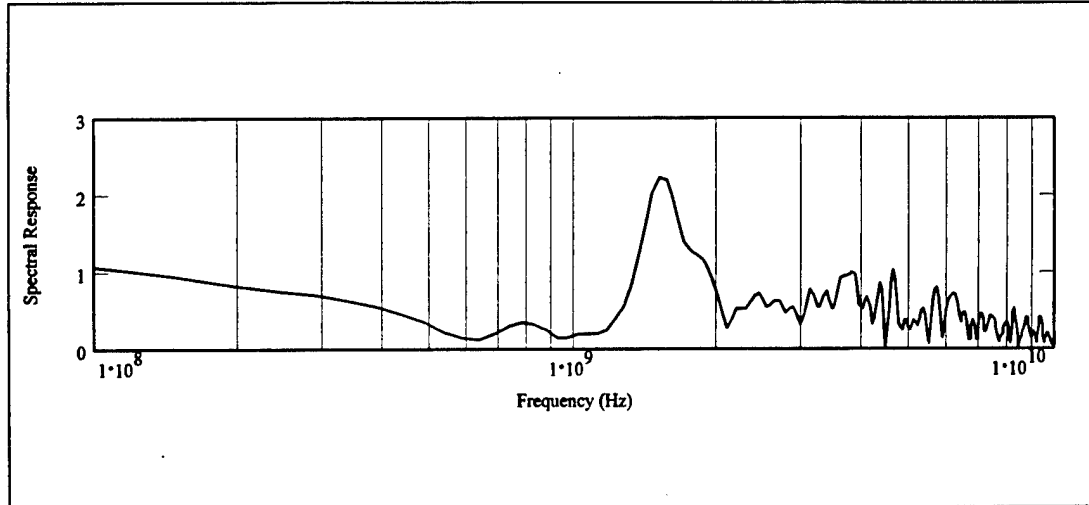


Figure 40. Fourier transform of the windowed difference waveform (same as figure 38).

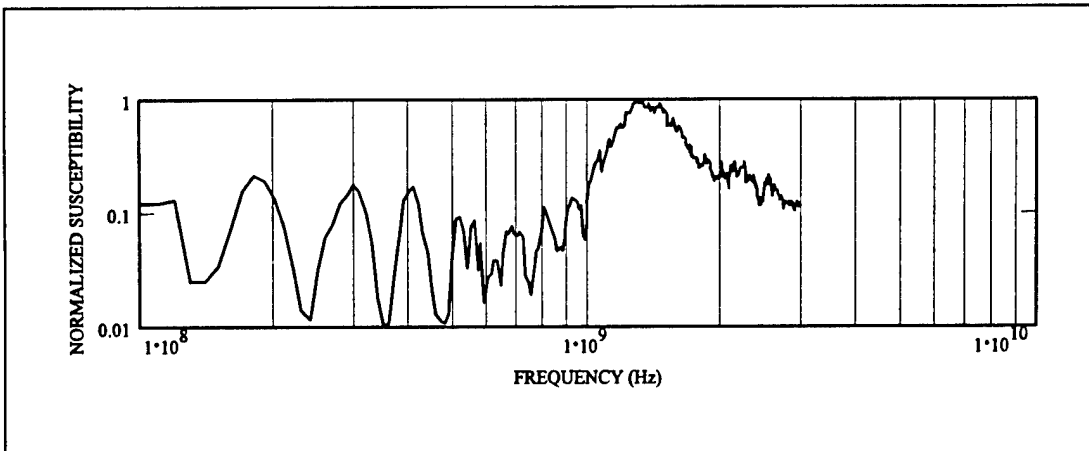


Figure 41. Normalized susceptibility (same as figure 24).

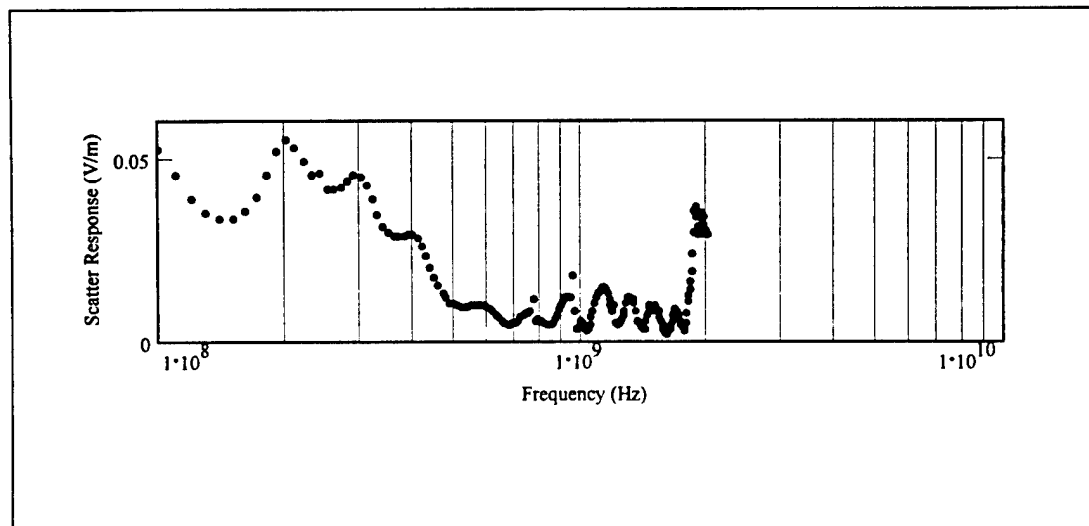


Figure 42. NEC 2 bistatic scatter analysis.

Table 5. Frequency errors, Δf_c

Mode	$n\lambda/2$ calculated	SEM calculated	NEC 2 computed	Impulse scattered	Coupling measured
Body modes (MHz)					
1	>+12.50*	<-11.50*	<-10*	*	0
2	+42.00	+7.60	+7	+13	0
3	+37.50	-4.30	-20	+3	0
4	+46.00	-1.40	-24	-13	0
5	+43.50	-8.30	+41	-11	0
Probe modes (MHz)					
1	+160 to -40	+13.33 to -186.70	not avail.	+240 to +40	0
2	*	*	not avail.	none	none

* cannot be determined.

Table 6. Percent bandwidth errors

Mode	$n\lambda/2$ calculated	SEM calculated	NEC 2 computed	Impulse scattered	Coupling measured
Body modes (MHz)					
1	*	*	*	*	0
2	84	16	14	26	0
3	64	8	34	6	0
4	78	2	40	22	0
5	128	24	120	32	0
Probe modes (MHz)					
1	<32	<38	*	<48	0
2	*	*	*	none	none

* cannot be determined.

7. Conclusions

Narrow band coupling and ultra-wide band scattering measurements were conducted on a pseudomissile. Two dominant coupling mechanisms were observed. The first was associated with region I, where the dominant coupling aperture was defined by the pseudomissile body. The second mechanism was associated with region II. This region consisted of the 5.15 cm long wire probe protruding from the 8.5 cm diameter end cap to the pseudomissile frustum. The dominant susceptibility occurred near the first mode of the pseudomissile's probe. In spite of being the dominant factor in the system's coupled response, this mode was not easily discernable in the scatter response's transfer function. These physical measurements have demonstrated the difficulty in isolating dominant frequency responses in the system's susceptibility profile. Significant numbers of higher modes were observed in the body response, but none were of obvious importance in defining the system's susceptibility. If this were an objective experiment in which the susceptibility of the system were not known in advance, there would have been tremendous ambiguity in the meaning of all the scatter modes observed.

Distinct resonances appeared in the scatter transfer function that corresponded to body modes of the system. These body modes extended well into the GHz region. An algorithm was presented in which the bistatic transfer function of the test object was accurately determined to within 10 percent of the center frequency.

The higher order modes decreased in intensity with increasing frequency. This seems to be a consequence of decreasing amplitude in the side lobes in the direction of the receive sensor. Specular scattering becomes dominant as the resonant region gives way to the Mie region.

A signal differencing technique was used to isolate the probe response from the grosser body response. A distinct frequency at 1.54 GHz was culled from the scatter signature. This was important in the case of the pseudomissile since the probe was responsible for the dominant susceptibility. However, the signal subtraction technique does not eliminate mutual interaction terms, which may account for the differenced waveform having a significantly higher frequency than expected of the missile probe and its perfect image.

The impulse scatter response of the pseudomissile contained susceptibility frequency information, provided a careful analysis was performed. Several

tools, techniques, and methods are presented in this paper. The tools used were a calibrated pseudomissile test asset, narrow band coupling measurements, and a custom designed impulse scattering system. The techniques employed both narrow band and ultra-wide band RF to establish a connection between the scattered and coupled spectra. Data analysis methods used include both Fourier and windowed Fourier transformation techniques, and a reference is given to work that was done for ARL by E. Walton. [2] It was found that by changing the pseudomissile's configuration (that is, the removal of the probe at the missile's tip), smaller but very important physical features of the missile system could be enhanced. Measurements were made before and after its removal. Signal differencing was applied to remove most of the unwanted response from the surrounding pseudomissile body. This method would be difficult to apply unambiguously to more complex systems that have retractable fins, fin slots, seams, apertures, and external cable runs. Mutual coupling terms still exist that cannot be subtracted. In order to account for these interaction terms, a better analysis technique must be applied to the scattered waveform.

8. Recommendations

The analysis of bistatic impulse scatter data and narrow band susceptibility data has shown that they are correlated for the specific experiment conducted on pseudomissile case I. Simple Fourier analysis was applied with good results. However, this could only be used for the lower frequency body modes. As was seen in isolating the probe response, a signal subtraction and "short-time" windowed transformation was necessary. Mutual coupling terms could not be removed with the windowing process.

Since EM coupling has a scaling property for linear systems dependent upon the local region's resonant modes, it is appropriate to consider an analysis in the light of recent developments in wavelet analysis or other time-frequency analysis techniques. Several types of analyses have been applied to a limited dataset. [2] These analyses consisted of the short-time, Wigner, wavelet, and a bi-time analysis. As yet, these analysis techniques have not been adequately explored to produce a definitive tool for the unambiguous identification of dominant susceptible frequencies. Only one short-time window has been explored. There are better windows and mother wavelets than are presently available that would enhance the signal extraction and frequency identification.

The results of this report show that frequencies of coupled fields are evident in the scatter signature of the pseudomissile. However, it is still unclear with the analysis presented in this paper that those modes that are significant in defining a system's susceptibility can be identified. Further exploration of signal processing, as well as physical measurement techniques in identifying frequencies to which a system may be susceptible, with the intention of applying the technique to a more complex system is necessary. To promote a methodical investigation of the scatter/couple relation and development of a more robust tool, further study of the increasingly complex pseudomissile (cases II - IV) is recommended. A series of techniques making use of this principle of selective enhancement or attenuation of specific system features (such as the removal or replacement of the pseudomissile probe) should be established by further experimental work on more complex systems. It was shown that using the impulse scatter techniques and methods described, the accuracy of frequency prediction for the pseudomissile is within 48 percent of the measured susceptible frequencies. This accuracy may be improved by better radiator/sensor selection, signal processing enhancements, and alternate wide band schemes such as swept narrow band measurement. By studying and comparing the scatter response versus narrow band coupling from more complex systems, the utility of the techniques can be improved.

References

1. Butler, Professor Chalmers, Clemson University, Memorandum, 27 October 1994.
2. Walton, Eric, *Time Frequency Distribution Analysis of EM Impulse Scattering from a Missile Shape*, Report Number TCN94287, March 1996.
3. Henderson, Jayme B., *RF Field Probe and Telemetry System*, working papers.
4. Wilson, Jay L. and Youn Moo Lee, *Missile Sensitive Frequency Program (MSFP) User's Manual*, Physical Science Laboratory, under contract DAAD07-79-C-0042, March 1981.
5. Melson, Gary Bruce and L. Wilson Pearson, *SEM Characterization of the Electromagnetic Scattering from Thin and Thick Open-Ended Cylinders*, University of Kentucky, under contract to the Physical Sciences Laboratory, Number 284, report 80-4, November 1980.
6. Collins, W. F. et. al., *SEMIVAF Level II Facility Documentation*, SLCVA-TM-87-11, October 1986.
7. White, Patricia and William Cooper, *Enhancements to Signal Processing Diagnostic Tools*, ARL-TR-543, Interim report, December 1994.
8. Cooper, William K. and Melinda M. Medd, *Data Acquisition Processing Reduction (DAPR) User's Manual*, prepared for ARL's Electromagnetic Analysis Facility, WSMR, NM, December 1994.
9. Morgan, Michael A., "Ultra-Wide Band Impulse Scattering Measurements," *IEEE Transactions on Antennas and Propagation*, Vol. 42, No. 6, June 1994.

Acronyms and Abbreviations

AMI	Automated Microwave Instrumentation
ARL	U.S. Army Research Laboratory
ASCII	American Standard Code for Information Interchange
BAMI	B version of the AMI
CW	continuous wave
DSO	digital sampling oscilloscope
EM	electromagnetic or electromagnetism
EMAF	Electromagnetic Analysis Facility
EMI	electromagnetic interference
EMP	electromagnetic pulse
EWVAF	Electromagnetic Vulnerability Assessment Facility
FFT	fast Fourier transform
FM	frequency modulation
IEPD	Information & Electronic Protection Division
J/S	jammer-to-signal ratio
MSFP	Missile Sensitive Frequency Program
NEC 2	Numerical Electromagnetic Code, version 2
RF	radio frequency
SEM	singularity expansion method
SLAD	Survivability/Lethality Analysis Directorate
TDM	time division multiplexing
TDR	time domain reflectometry or time domain reflectometer
TEM	transverse electromagnetic
TM	telemetry
WSMR	White Sands Missile Range
Ω	ohm

Appendix A
D-dot Signal Integration Scaling
and Correction

Worksheet: D_dot_integration.MCD

This MathCAD worksheet corrects the measured waveform retrieved from a D-dot field probe to produce an approximate facsimile of the incident waveform.

$D = \text{READPRN}(\text{shot449d})$ Read incident shot data file. This data is plotted in figure A.1.
 $D_{1023,1} = D_{1022,1}$ $D_{1023,0} = D_{1022,0} + D_{0,0}$ Pad lost data point on end of record.
 $i = 0..1023$ Data index.

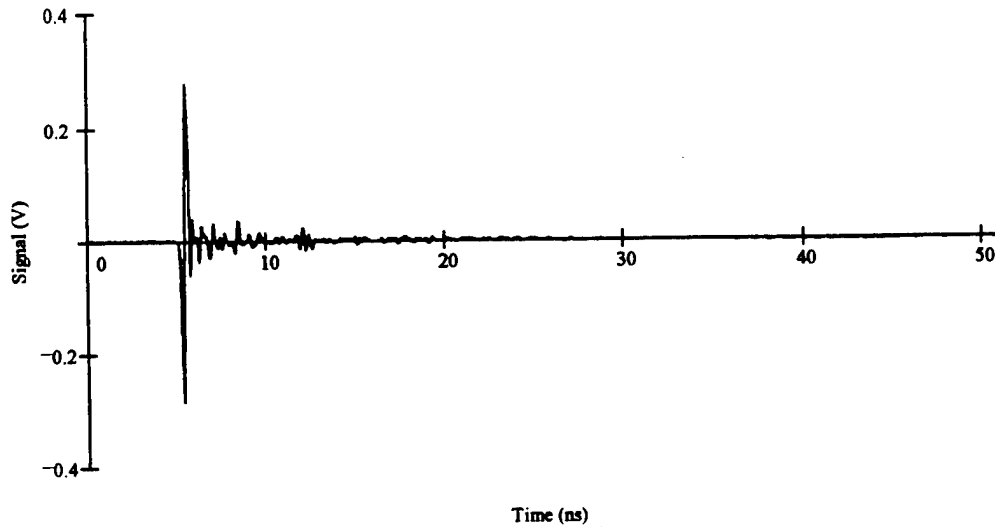


Figure A.1. Uncorrected sensor signal.

$$\Delta t = D_{1,0}$$

$$\text{Attn} = 10$$

$$Z_s = 50$$

$$A_{\text{eff}} = 10^{-3}$$

$$\epsilon_0 = 8.854 \cdot 10^{-12}$$

$$A = \begin{cases} A_0 - D_{0,1} \\ \text{for } k \in 1..1022 \\ A_k - A_{k-1} + 2 \cdot D_{k,1} \\ A_{1023} - A_{1022} + D_{1023,1} \\ \frac{\text{Attn}}{Z_s \cdot A_{\text{eff}} \epsilon_0} \cdot \frac{\Delta t \cdot 10^{-9}}{2} \end{cases}$$

Sample period.

Attenuation factor due to a 20 dB pad in line (note that the attenuation given is in linear units).

Sensor impedance

Sensor effective area.

Dielectric permittivity of free space.

Integrate the D-dot response using the trapezoidal sample approximation. The integrated and scaled waveform is shown in figure A.2.

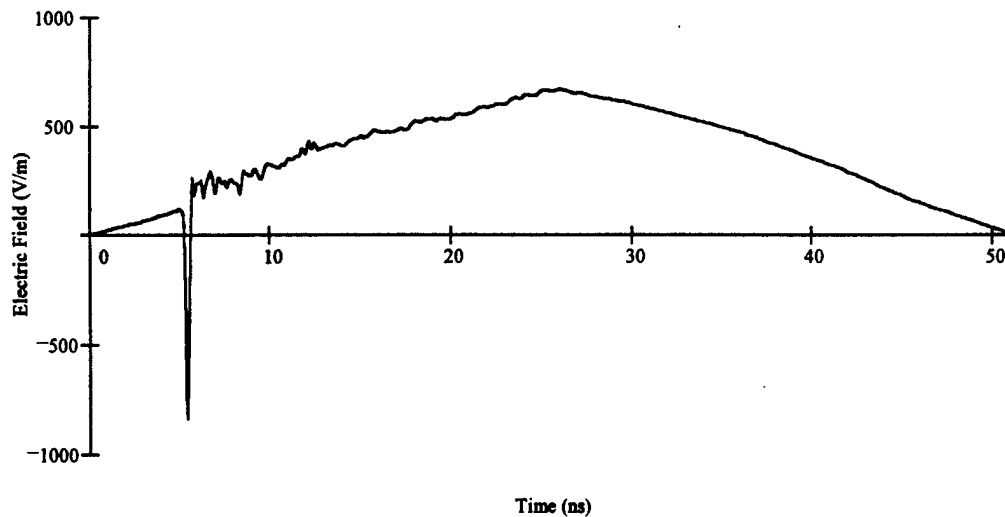


Figure A.2. Integrated and scaled sensor signal without cable correction.

The signal has been converted to the incident electric field, but has a noncausal (hence nonphysical) bowing in its shape. The large anechoic chamber has an effective lower anechoic frequency of 100 MHz. The TEM antenna's radiation efficiency also declines significantly below the resonant length of its radiating blades. Combined with the increasing inefficiency of the D-dot field probe indicates that applying a high pass filter with a 100 MHz cutoff frequency is appropriate. This is done as follows:

$$\Delta f := \frac{1}{51.15 \cdot 10^{-9}}$$

$$\text{setwindow}(6) = 6$$

$$\text{order} := 2 \quad \epsilon := 0.5$$

Define 2nd order with passband ripple of 0.5 dB.

$$\text{nf} := \frac{51.15 \cdot 0.10}{1024} \quad \text{nf} = 0.005$$

Normalized cutoff frequency corresponding to 100 MHz.

$$\text{nf} \cdot 1024 \cdot \Delta f = 1 \cdot 10^8$$

Cutoff frequency is 100 MHz

$$\text{coef} := \text{iirhigh}(\text{cheby1}(\text{order}, \epsilon), \text{nf})$$

Compute the Chebychev type I highpass filter coefficients

$$\text{res}^{<1>} := \text{response}(A, \text{coef}, 1024)$$

Compute the highpass filtered response. (See figure A.4.)

$$\text{RES} := \text{FFT}(\text{res}^{<1>})$$

Compute FFT of the filtered signal. (See figure A.3.)

$$j := 0..512$$

Fast Fourier transform is symmetric so define a new index for half the number of elements.

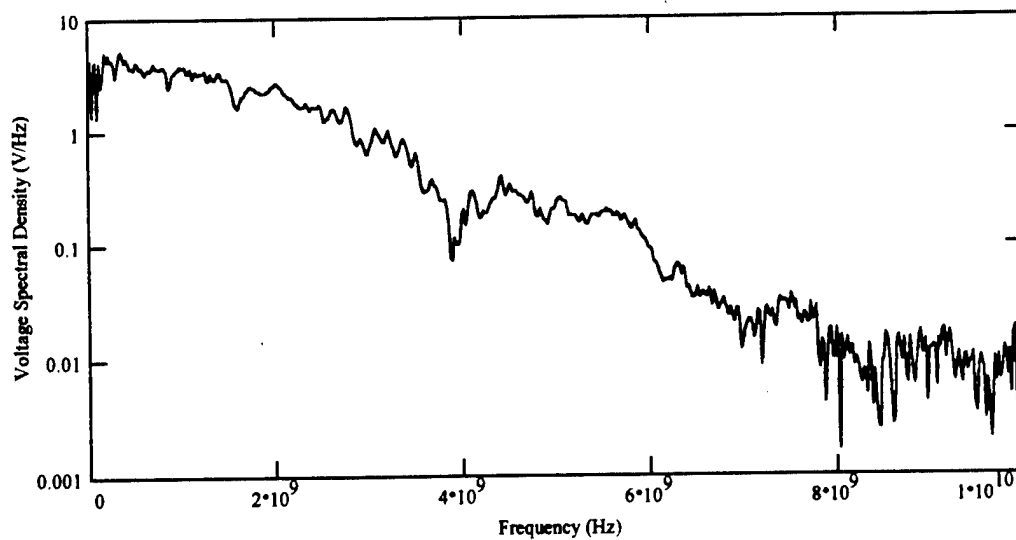


Figure A.3. High-pass filtered signal spectrum.

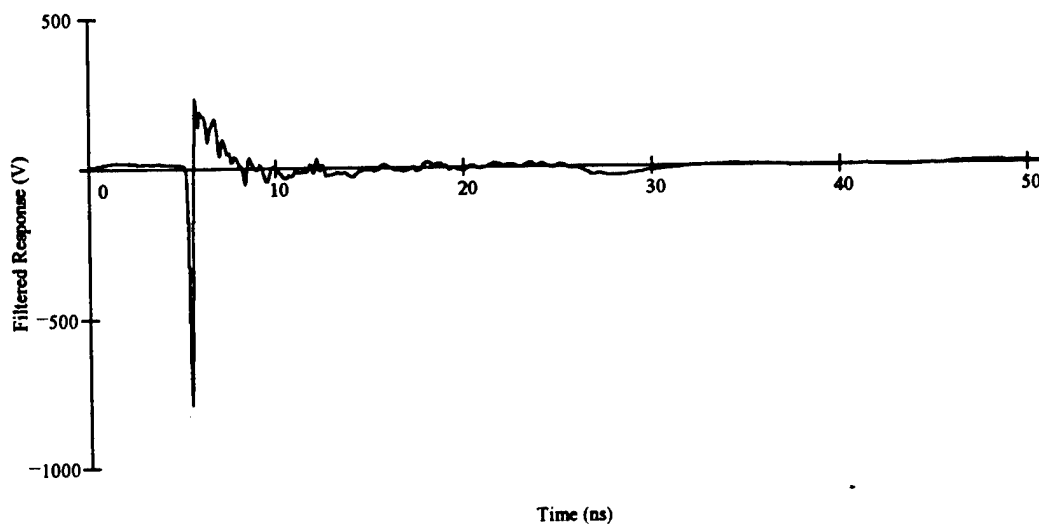


Figure A.4. High-pass filtered signal.

`res<0> = D<0>`

Assign the time series to the amplitude record.

`WRITEPRN(Incident_DAT) = res0`

Write the integrated and filtered time record to disk.

As discussed in the main text, cable corrections are not necessary since their effect is compensated for in the deconvolution algorithm. However, their effect is considered here in order to better understand their effect on transient pulses.

A 20 ft coaxial cable was measured with a Wiltron scalar network analyzer (SNA) for loss. It is assumed that the cable has a linear phase characteristic across to operating band under consideration. The measurement results are as follows.

$A := \text{READPRN}(\text{CABLE_DAT})$ Measure the cable plus SNA S_{12} transmission characteristics.

$B := \text{READPRN}(\text{BKGND1_DAT})$ Measure the SNA S_{12} transmission characteristics only.

$k := 0.. \text{length}(A^{<0>}) - 1$ Define an indexing variable.

The SNA and SNA+Cable S_{12} loss measurement data are plotted in figure A.5.

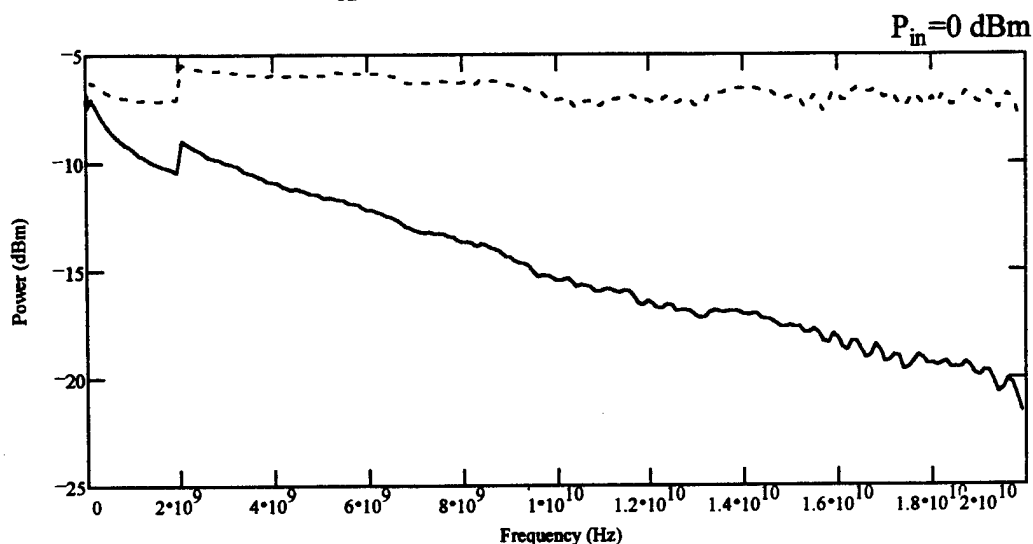


Figure A.5. SNA (dotted line) and SNA+cable (solid line) S_{12} parameters.

$C^{<1>} := A^{<1>} - B^{<1>}$ Subtract background from cable.

$$\Delta f := \frac{1}{51.15 \cdot 10^{-9}}$$

$C^{<0>} := A^{<0>}$ Assign frequency series to $C^{<0>}$ vector.

$k1 := 0..1023$ Data index.

$Cl_{k1} := \text{linterp}(C^{<0>}, C^{<1>}, \Delta f \cdot k1)$ Regularize the cable data points. This data is plotted in figure A.6.

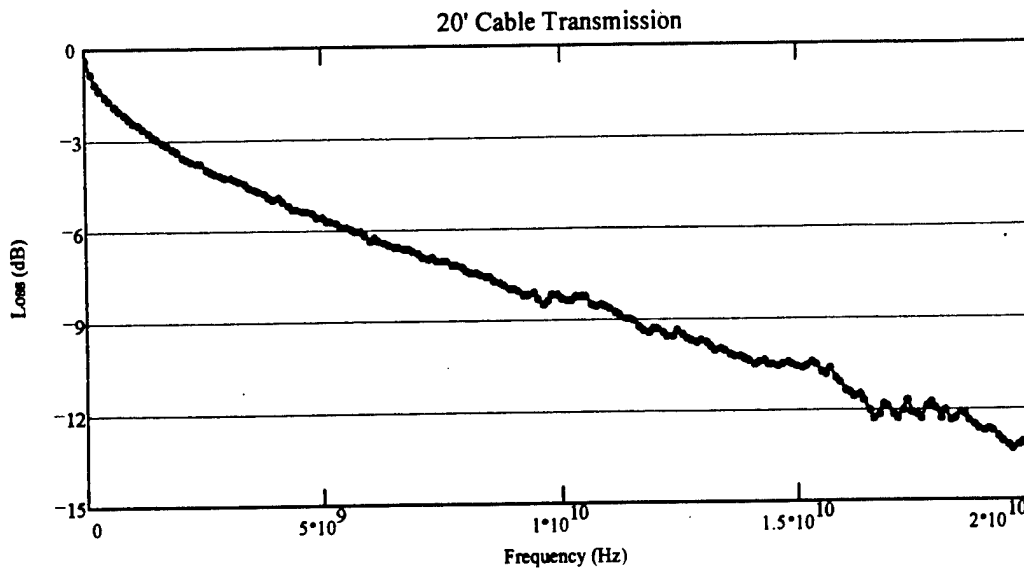


Figure A.6. Cable loss transfer function (magnitude only) for measured (dotted) and interpolated (solid) values.

$$C_{lin_i} = 10^{\frac{CI_i}{20}}$$

Linearize the cable loss transfer function magnitude (no phase information is available from the Wiltron scalar network analyzer from which this data was taken).

$$FA = FFT(res^{<1>})$$

Compute the Fourier transform of the measured incident signal. This spectrum is plotted in figures A.7 and A.8.

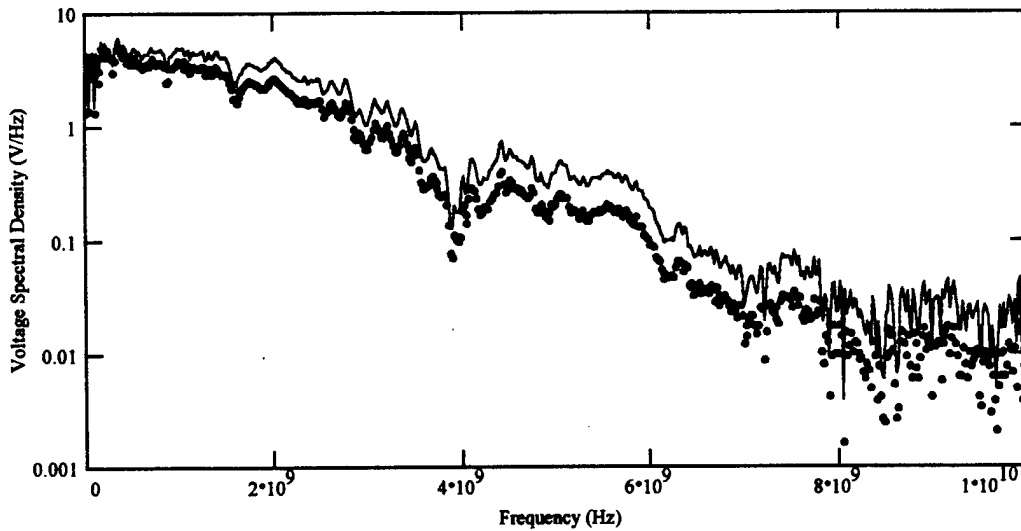


Figure A.7. Uncompensated (dotted line) and compensated (solid line) incident field spectral magnitudes.

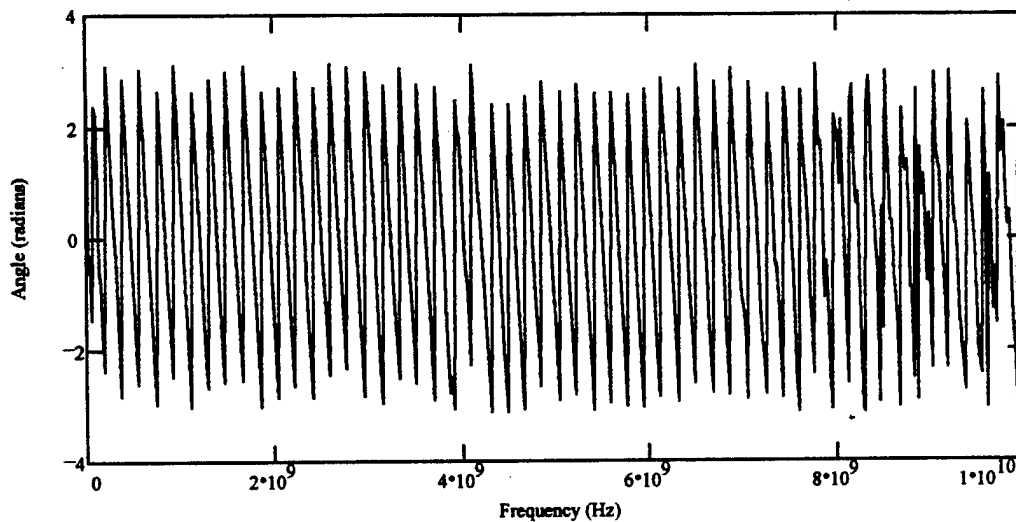


Figure A.8. Uncompensated spectral phase.

$$FE_j = \frac{|FA_j|}{C_lin_j} \cdot (\cos(\arg(FA_j)) + i \cdot \sin(\arg(FA_j)))$$

Correct for cable losses (neglecting phase).

$$E = \text{IFFT}(FE)$$

Compute inverse Fourier transform. This reproduces the corrected Electric-field density incident at the D-dot sensor location, hence the field incident upon the pseudomissile.

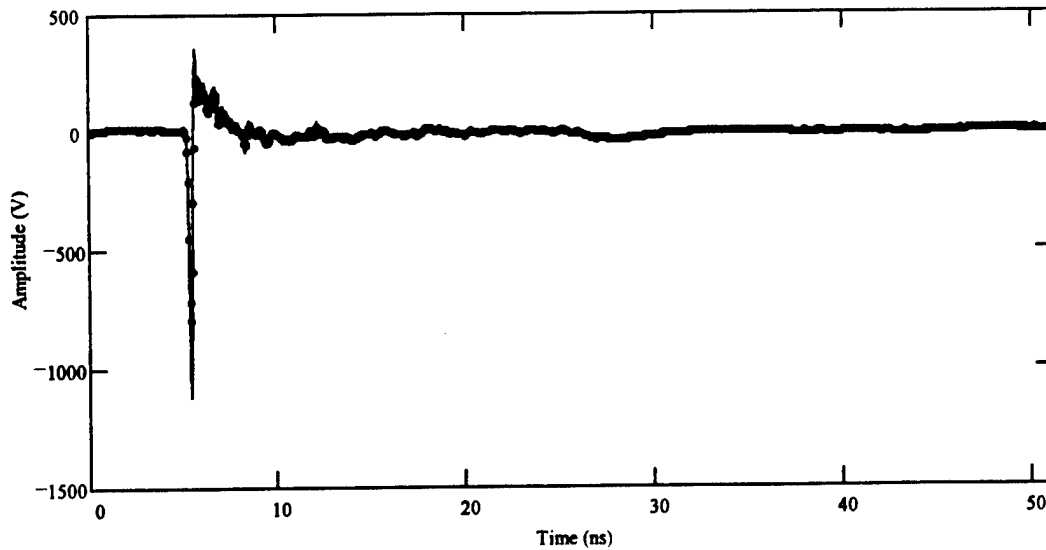


Figure A.9. Uncompensated cable (dotted line) and compensated (solid line) transient pulse incident at center of azimuth positioner.

Figure A.9 shows that the incident impulse at the center of the azimuth positioner is -1100 V/m in magnitude with a 10% to 90% rise time of ~200 picoseconds. The spectral energy of this pulse begins to become noisy at 7.5 GHz as indicated in the phase figure A.8. This is interesting since the D-dot field probe is only specified for frequencies up to 3 GHz.

Appendix B

Background Subtraction

Worksheet: bkgnd_sbtrct.MCD

8 October 1996

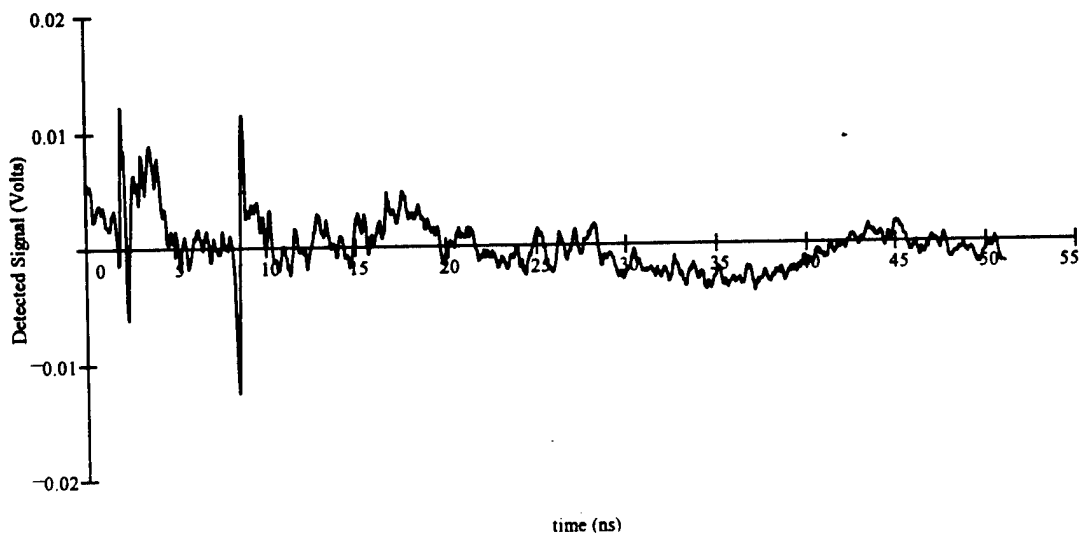
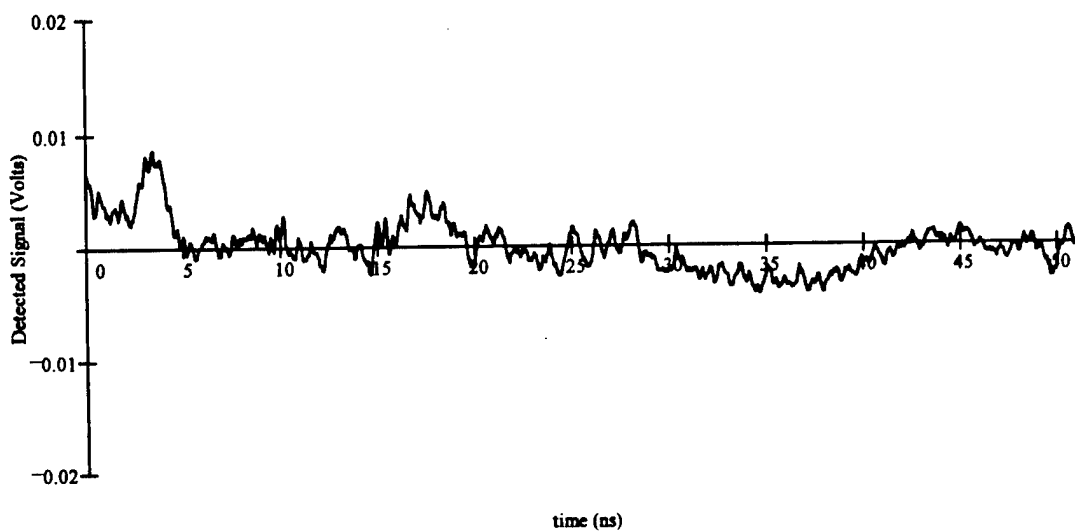
Description: This worksheet reads two signal files from disk formatted as 2 column ASCII. The second column vector of the second file is point by point subtracted from the second column vector of the second column vector of the first file.

A := READPRN(shot524d) Read background+scatter file.

B := READPRN(shot450d) Read background file.

i = 0..1022

A_{1023,0} = 51.15 A_{1023,1} = A_{1022,1} B_{1023,0} = 51.15 B_{1023,1} = B_{1022,1} Define last point.

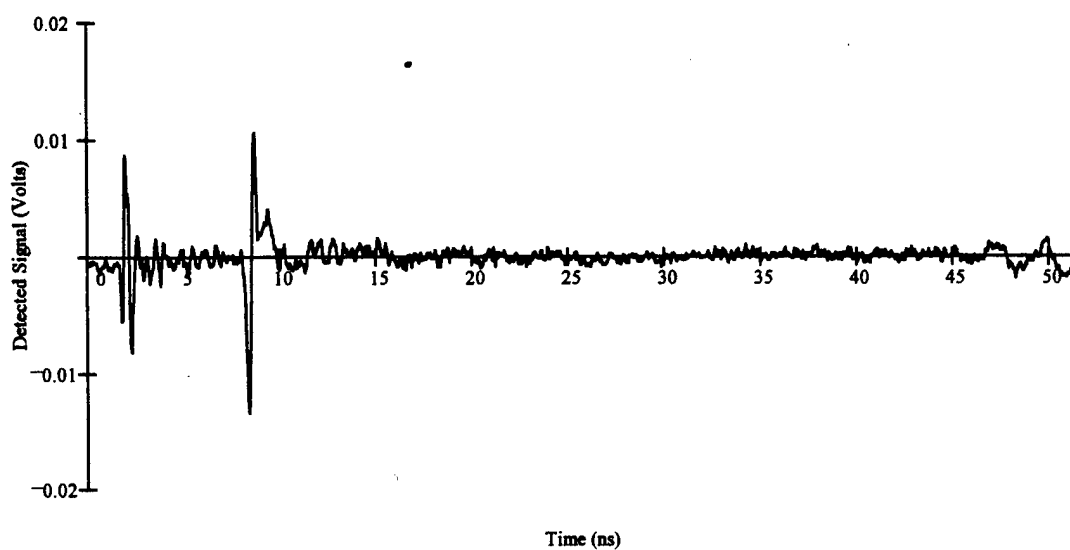


$$C_{i,1} := A_{i,1} - B_{i,1}$$

Subtract the background voltage from the background+scatter superposed voltage.

$$C_{i,0} := B_{i,0}$$

Keep the time scale.



$$\text{WRITEPRN}(\text{SB524}) := C_0$$

Write the background subtracted waveform to a new file.

Appendix C

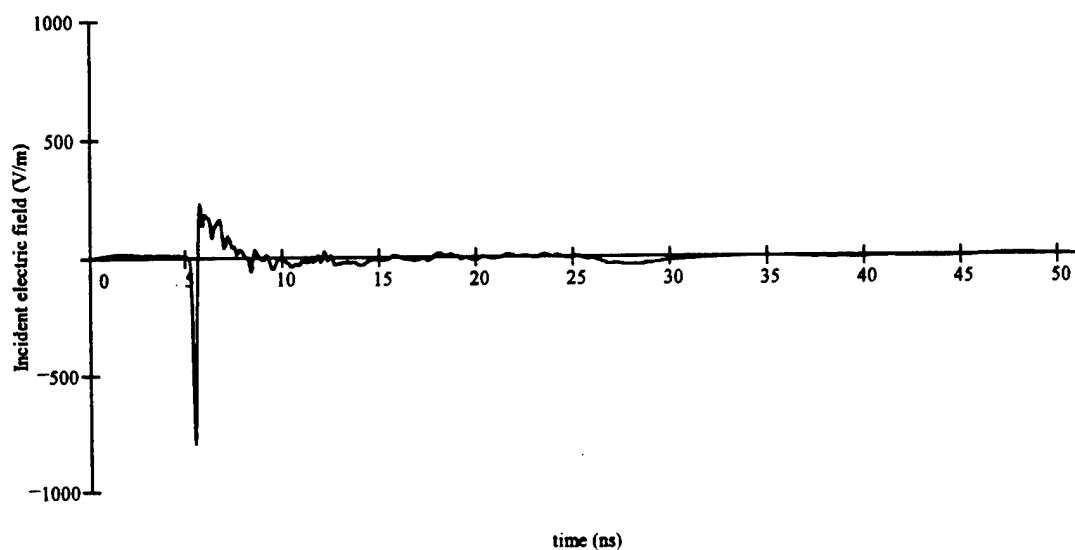
Normalization

Worksheet: Normalization.MCD

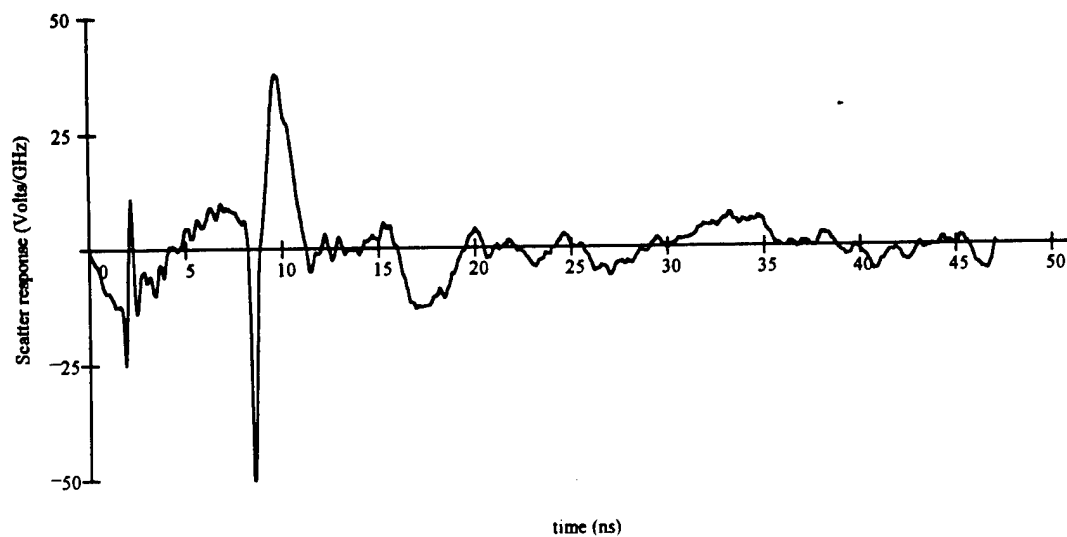
10 Oct. 1996 JBH

Description: This worksheet reads in both an incident waveform and a scattered waveform and computes the scatter body's transfer function.

$$A = \text{READPRN}(\text{ISB524.dat}) \quad B = \text{READPRN}(\text{INCIDENT.dat}) \quad \Delta f = \frac{1}{51.15 \cdot 10^{-9}} \quad i = 0..1023$$



$$j = 940..1023 \quad A_{j,1} = 0$$

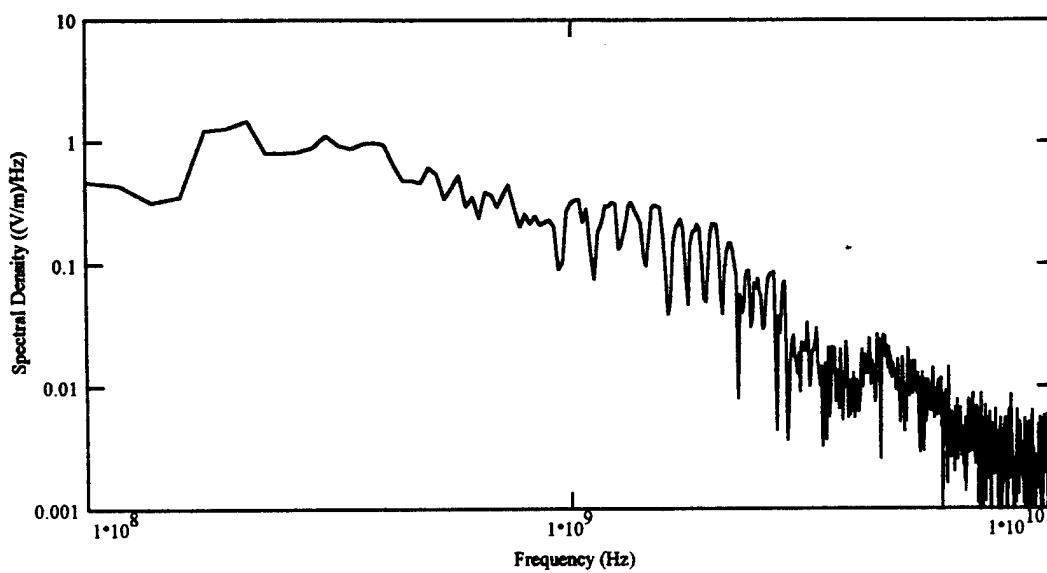
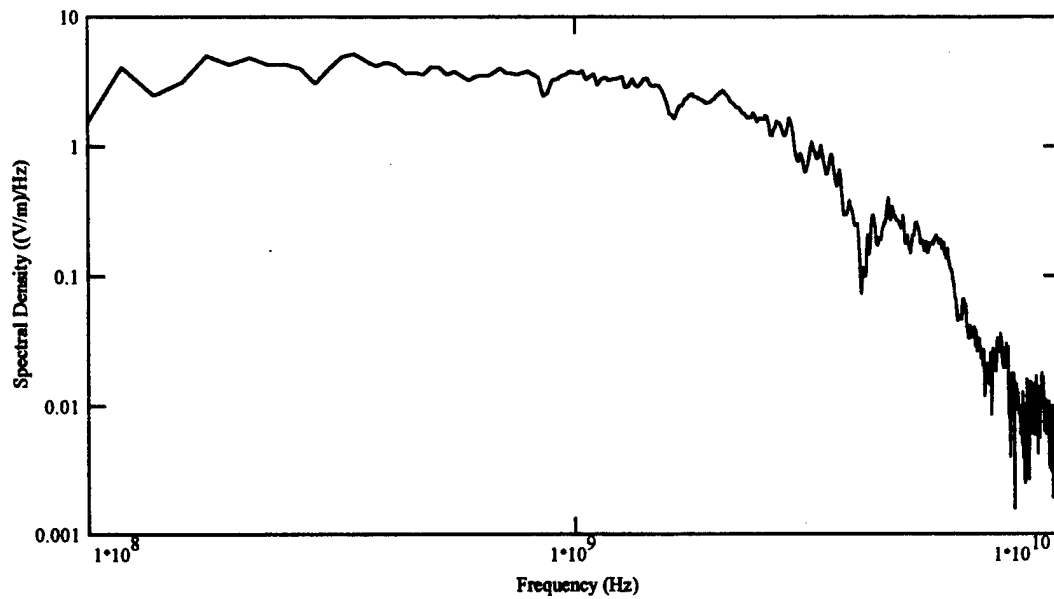


FB := FFT(B<1>) Fourier transform the incident waveform.

j2 := 2..510

FA := FFT(A<1>) Fourier transform the scattered waveform.

j := 0..512



$$\text{Mag_N}_j = \frac{|FA_j|^2}{(|FB_j|^2 + 0.15)}$$

Compute Transfer function magnitude.

$$\text{Pha_N}_j = (\arg(FA_j) - \arg(FB_j)) - j \cdot 0.65$$

Compute Transfer function phase with linear phase shift.

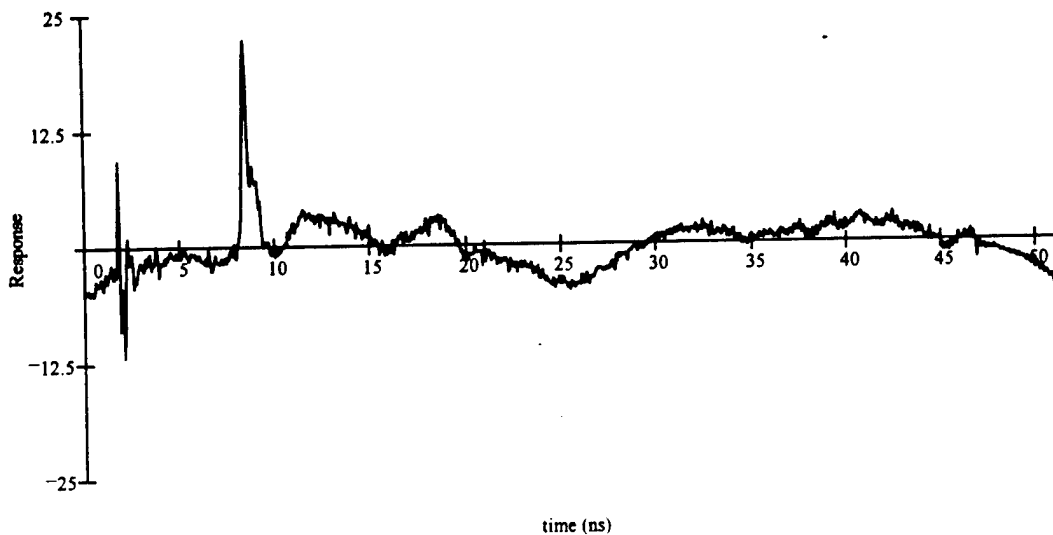
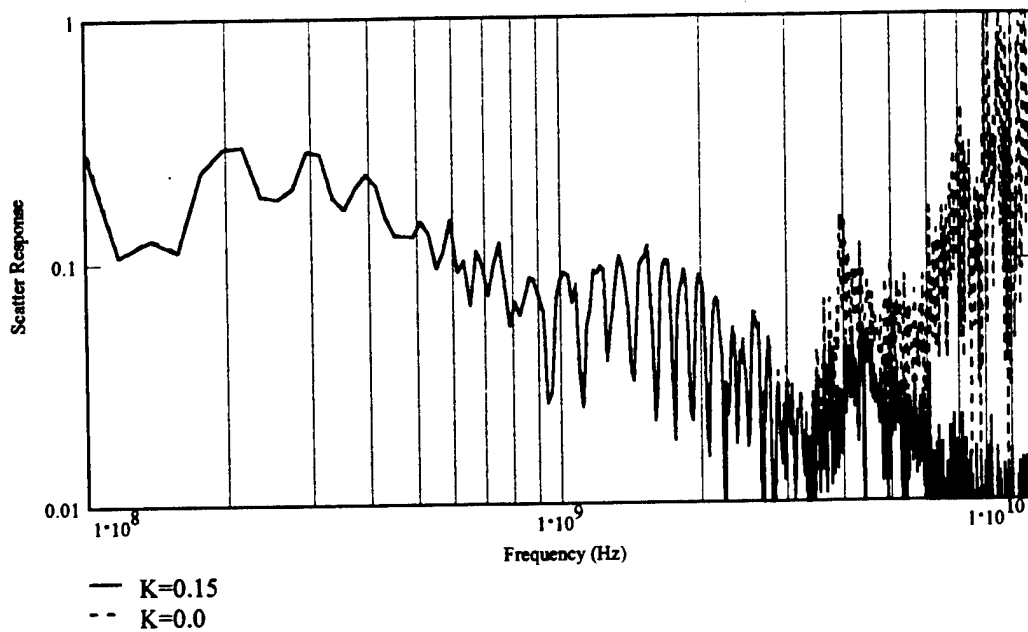
$$\text{FN}_j := \sqrt{\text{Mag_N}_j} \cdot e^{j \cdot \text{Pha_N}_j}$$

Convert the normalized Transfer function into complex (x,y) form.

$$N = \text{IFFT}(\text{FN})$$

Compute Normalized impulse response.

i2 = 1..1023



Distribution

	Copies
DEFENSE TECH INFO CTR ATTN DTIC OCA J CHIRAS 8725 JOHN J KINGMAN RD STE 0944 FT BELVOIR VA 22060-6218	2
OUSD AT S&T AIR WARFARE ATTN DR RAINIS RM 3E139 3090 DEFENSE PENTAGON WASHINGTON DC 20310-3090	1
OUSD AT S&T LAND WARFARE ATTN MR VILU RM 3B1060 3090 DEFENSE PENTAGON WASHINGTON DC 20310-3090	1
OASD C31 ATTN DR SOOS RM 3E194 6000 DEFENSE PENTAGON WASHINGTON DC 20301-6000	1
UNDER SEC OF THE ARMY DUSA OR RM 2E660 102 ARMY PENTAGON WASHINGTON DC 20310-0102	1
ASST SECY ARMY RESEARCH DEVELOPMENT ACQUISITION SARD ZD RM 2E673 103 ARMY PENTAGON WASHINGTON DC 20310-0103	1
ASST SECY ARMY RDA SARD TT RM 3E479 ATTN DR MILTON 103 ARMY PENTAGON WASHINGTON DC 20310-0103	1
ASST SECY ARMY RESEARCH DEVELOPMENT ACQUISITION SARD ZP RM 2E661 103 ARMY PENTAGON WASHINGTON DC 20310-0103	1

ASST SECY ARMY RESEARCH DEVELOPMENT ACQUISITION SARD ZS RM 3E448 103 ARMY PENTAGON WASHINGTON DC 20310-0103	1
OADCOPS FORCE DEV DIR ATTN DAMO FDW RM 3C630 460 ARMY PENTAGON WASHINGTON DC 20310-0460	1
OADCOPS FORCE DEV DIR ATTN DAMO FDT MR DENNIS SCHMIDT 460 ARMY PENTAGON WASHINGTON DC 20310-0460	1
US MILITARY ACADEMY MATH SCI CTR EXCELLENCE ATTN MADN MATH LTC ENGEN THAYER HALL WEST POINT NY 10996-1786	1
HQ USAMC DEP CHF OF STAFF FOR RDA ATTN AMCRDA 5001 EISENHOWER AVE ALEXANDRIA VA 22333-0001	1
HQ USAMC PRINCIPAL DEP FOR ACQSTN ATTN AMCDCG A 5001 EISENHOWER AVE ALEXANDRIA VA 22333-0001	1
HQ USAMC PRINCIPAL DEP FOR TECH ATTN AMCDCG T 5001 EISENHOWER AVE ALEXANDRIA VA 22333-0001	1
ARMY TEST EVAL COM AMSTE TM S APG MD 21005-5055	1
US ARMY EVAL ANALYSIS CTR ATTN CSTE EAC MR HUGHES 4120 SUSQUEHANNA AVE APG MD 21005-3013	1

US ARMY EVAL ANALYSIS CTR ATTN CSTE EAC SV DR HASKELL 4120 SUSQUEHANNA AVE APG MD 21005-3013	1
ARMY TRNG & DOCTRINE COM ATTN ATCD B FT MONROE VA 23561-5000	1
ARMY TRADOC ANL CTR ATTN ATRC W MR KEINTZ WSMR NM 88002-5502	1
ARMY RESEARCH LABORATORY ATTN AMSRL ST DR ROCCHIO 2800 POWDER MILL RD ADELPHI MD 20783-1197	1
ARMY RESEARCH LABORATORY ATTN AMSRL SL DR WADE APG MD 21005-5068	1
ARMY RESEARCH LABORATORY ATTN AMSRL SL PLANS AND PGMS MGR WSMR NM 88002-5513	1
ARMY RESEARCH LABORATORY ATTN AMSRL SL-E DR STARKS APG MD 21010-5423	1
ARMY RESEARCH LABORATORY ATTN AMSRL SL B LTC GILMAN APG MD 21005-5068	1
ARMY RESEARCH LABORATORY ATTN AMSRL SL MR BEILFUSS APG MD 21005-5068	1
ARMY RESEARCH LABORATORY ATTN AMSRL SL E MR SHELBURNE WSMR NM 88002-5513	1
ARMY RESEARCH LABORATORY ATTN AMSRL CS AL TA 2800 POWDER MILL RD ADELPHI MD 20783-1145	1

ARMY RESEARCH LABORATORY ATTN AMSRL CS AL TP 2800 POWDER MILL RD ADELPHI MD 20783-1145	1
ARMY RESEARCH LABORATORY ATTN AMSRL CI LL 2800 POWDER MILL RD ADELPHI MD 20783-1145	3
ARMY RESEARCH LABORATORY ATTN AMSRL CI LP BLDG 305 ABERDEEN MD 21005-5068	2
US ARMY RESEARCH OFFICE ATTN AMXRO EL DR JAMES HARVEY PO BOX 12211 RESRCH TRI PK NC 27709-2211	1
DERA PROF DAVID PARKS ST ANDREWS RD MALVERN WORCHESTER WR143PS	3
NMSU DEPT OF ELECT & COMP ENG DR. JAY JORDAN LAS CRUCES NM 88003	1
REAP ATTN DR GLENN BROWN 5937 VIA ROBLES LANE EL PASO TEXAS 79912	1
CLEMSON UNIVERSITY DEPT OF ELEC AND COMP ENG CHALMERS M BUTLER 201 RIGGS HALL CLEMSON SC 29634-0915	1
ARMY RESEARCH LABORATORY ATTN AMSRL SL EM MR HENDERSON WSMR NM 88002-5502	10
Record Copy	2
Total	54